GEOFLUIDS

Geofluids (2015) **15**, 269–292 doi: 10.1111/gfl.12110

An analytical solution for solitary porosity waves: dynamic permeability and fluidization of nonlinear viscous and viscoplastic rock

J. A. D. CONNOLLY[1] AND Y. Y. PODLADCHIKOV[2]

[1]*Department of Earth Sciences, Swiss Federal Institute of Technology, Zurich, Switzerland;* [2]*Earth Sciences Department, University of Lausanne, Lausanne, Switzerland*

ABSTRACT

Porosity waves are a mechanism by which fluid generated by devolatilization and melting, or trapped during sedimentation, may be expelled from ductile rocks. The waves correspond to a steady-state solution to the coupled hydraulic and rheologic equations that govern flow of the fluid through the matrix and matrix deformation. This work presents an intuitive analytical formulation of this solution in one dimension that is general with respect to the constitutive relations used to define the viscous matrix rheology and permeability. This generality allows for the effects of nonlinear viscous matrix rheology and disaggregation. The solution combines the porosity dependence of the rheology and permeability in a single hydromechanical potential as a function of material properties and wave velocity. With the ansatz that there is a local balance between fluid production and transport, the solution permits prediction of the dynamic variations in permeability and pressure necessary to accommodate fluid production. The solution is used to construct a phase diagram that defines the conditions for smooth pervasive flow, wave-propagated flow, and matrix fluidization (disaggregation). The viscous porosity wave mechanism requires negative effective pressure to open the porosity in the leading half of a wave. In nature, negative effective pressure may induce hydrofracture, resulting in a viscoplastic compaction rheology. The tubelike porosity waves that form in such a rheology channelize fluid expulsion and are predicted by geometric argumentation from the one-dimensional viscous solitary wave solution.

Key words: analytic solution, dynamic permeability, fluidization, lower crust, non-linear viscous, porosity waves

Received 19 February 2014; accepted 28 August 2014

Corresponding author: James A. D. Connolly, Department of Earth Sciences, Swiss Federal Institute of Technology, 8092 Zurich, Switzerland.
Email: james.connolly@erdw.ethz.ch. Tel: +41 44 632 7804. Fax: +41 44 632 1027.

Geofluids (2015) **15**, 269–292

INTRODUCTION

Many geological processes involve the expulsion of pervasively distributed fluids, as in the case of fluids trapped during sedimentation or fluids generated by partial melting and metamorphic devolatilization. Given the high elastic strength characteristic of rocks, efficient fluid expulsion requires irreversible deformation by time-dependent (viscous) or time-independent (plastic) mechanisms (Neuzil 2003; Gueguen *et al.* 2004). Models for ductile plastic compaction (cataclasis) reproduce the near-surface porosity profiles of sedimentary basins (Shi & Wang 1986; Audet & Fowler 1992), but creep is regarded as essential to deeper compaction processes (McKenzie 1987; Birchwood & Turcotte 1994; Fowler & Yang 1999). For such processes, permeability is a dynamic property that is determined by the interaction between rheology and the inherent gravitational instability of the intermingling of rock and fluids with different densities. This interaction may give rise to a hydrologic regime in which flow is accomplished by self-propagating domains of fluid-filled porosity (Fowler 1984; Richter & McKenzie 1984; Scott & Stevenson 1984). These domains, or porosity waves, correspond to steady-state solutions, that is, solutions in which the waves propagate with unchanging form, of the equations governing fluid flow through a viscous matrix. The intent of this study is to develop and explore an intuitive analytical solution for these waves that is general with

respect to the constitutive laws chosen to characterize the viscous rheology and permeability of the rock matrix.

There are numerous formulations of the equations governing compaction of a two-phase viscous system consisting of a porous rock matrix saturated with a less viscous interstitial fluid in the geological literature (McKenzie 1984; Scott & Stevenson 1984; Bercovici *et al.* 2001). These formulations differ primarily in the choices of constitutive relations and independent variables. Analytical solutions for solitary waves that develop according to these formulations have been published (Barcilon & Richter 1986; Rabinowicz *et al.* 2002; Richard *et al.* 2012), but assume linear viscous behavior. This limitation is potentially important in the context of fluid flow in the lower crust because the viscous response of crustal rocks is expected to be nonlinear (Kohlstedt *et al.* 1995; Ranalli 1995). A nonlinear viscous formulation is of broad interest because it defines the length scale on which lower crustal fluid flow patterns may deviate from gravitationally controlled flow. The compaction length is also important in that it defines the spatial scale for porosity. Thus, although porosity conjures up an image of grain-scale structures, it may apply to substantially larger features, such as fractures, provided these features are hydraulically connected and small in comparison with the compaction length.

Shortly after the recognition of porosity waves as a potential fluid transport mechanism in geologic systems, it was shown that the planar, sill-like, waves predicted from one-dimensional (1-d) formulations of the governing equations were unstable with respect to spherical waves in two- and three-dimensional (3-d) space (Scott & Stevenson 1986; Barcilon & Lovera 1989; Wiggins & Spiegelman 1995). Despite this result, the present analysis is restricted to the 1-d case because it provides a lower limit on the efficacy of compaction-driven fluid expulsion and because the characteristics of the 1-d waves converge rapidly with those of 3-d waves for the geologically interesting case of large amplitude waves (Connolly & Podladchikov 2007). With this restriction, there are three compaction-driven flow regimes that may arise as a consequence of a perturbation to the flux of an initial regime of steady flow through a matrix with uniform porosity (Fig. 1). If the perturbation is small, the steady-state solution is a periodic wave that degrades to a uniform increased porosity once the perturbation is eliminated. For larger perturbations, the steady-state is a solitary wave. Once nucleated, the solitary wave is non-dissipative and independent of its source. Thus, the solitary wave solution defines a steady-state regime in which flow is accomplished by self-propagating waves. Because the solitary wave amplitude is proportional to the intensity of perturbation, large perturbations may cause the matrix to disaggregate to a fluidized suspension. The analytic solution outlined here is used to define the conditions for these regimes.

The solitary wave regime is one in which the fluid flows through a coherent solid matrix, whereas in the fluidized regime the solid is suspended within, and carried by, the fluid, as in a granitic magma so that the suspension behaves as a single phase that is transported through dikes or as diapirs (Vigneresse *et al.* 1996). Although peripheral to the scope of this study, the generation of granitic melts by partial melting of the lower crust is a prominent example of fluidization in ductile rock. Unless melting is so extensive that it forms a magmatic suspension directly, a segregation mechanism is required to amplify melt fractions to the level required for transport by dikes or diapirs. Given the common occurrence of oriented vein-like segregations (Brown 2010), attention in the compaction literature has focused on the role of shear-enhanced melt segregation (Stevenson 1989; Holtzman *et al.* 2003; Rabinowicz & Vigneresse 2004). While melt segregation is not explored in this study, the mechanism of fluidization discussed here is distinct in that low melt fractions can be amplified to a suspension even under isostatic conditions. Such a mechanism may be relevant in the formation of large-scale diatexite migmatites, which record a wholesale evolution from unmelted source rock to granitic magma (Sawyer 1998; Milord *et al.* 2001).

The mechanism responsible for porosity waves in a viscous matrix is implicit in the conventional view of the mechanics responsible for compaction profiles in active sedimentary basins (Hunt 1990; Japsen *et al.* 2011) and the partially molten region beneath mid-ocean ridges (Forsyth *et al.* 1998). In both of these settings, which span the physical conditions of the lower crust, compaction is thought to maintain near-eustatic porosity-depth profiles in rocks that are moving relative to the Earth's surface. In the case of sedimentary basins, the rock matrix moves downward relative to surface due to burial, whereas at mid-ocean ridges, the rock matrix rises toward the surface as a consequence of mantle upwelling. The distinction between these scenarios and that of a porosity wave is no more than a matter of reference frame, in that in the former porosity is eustatic and the rock matrix moves, while in the latter, the rock matrix is largely stationary and the porosity moves. Indeed, mechanical models that explain eustatic porosity in sedimentary basins (Fowler & Yang 1999; Connolly & Podladchikov 2000) and at mid-ocean ridges (Katz 2008) differ trivially from the simple viscous formulation employed here. Specifically, for sedimentary basins a viscoplastic rheology is introduced to account for near-surface compaction, and for mid-ocean ridges, the model is modified to account for fluid production. The existence of porosity waves in a viscous matrix has also been demonstrated experimentally by mechanical analog (Olson & Christensen 1986; Scott *et al.* 1986; Helfrich & Whitehead 1990). Thus, suggestions that porosity waves

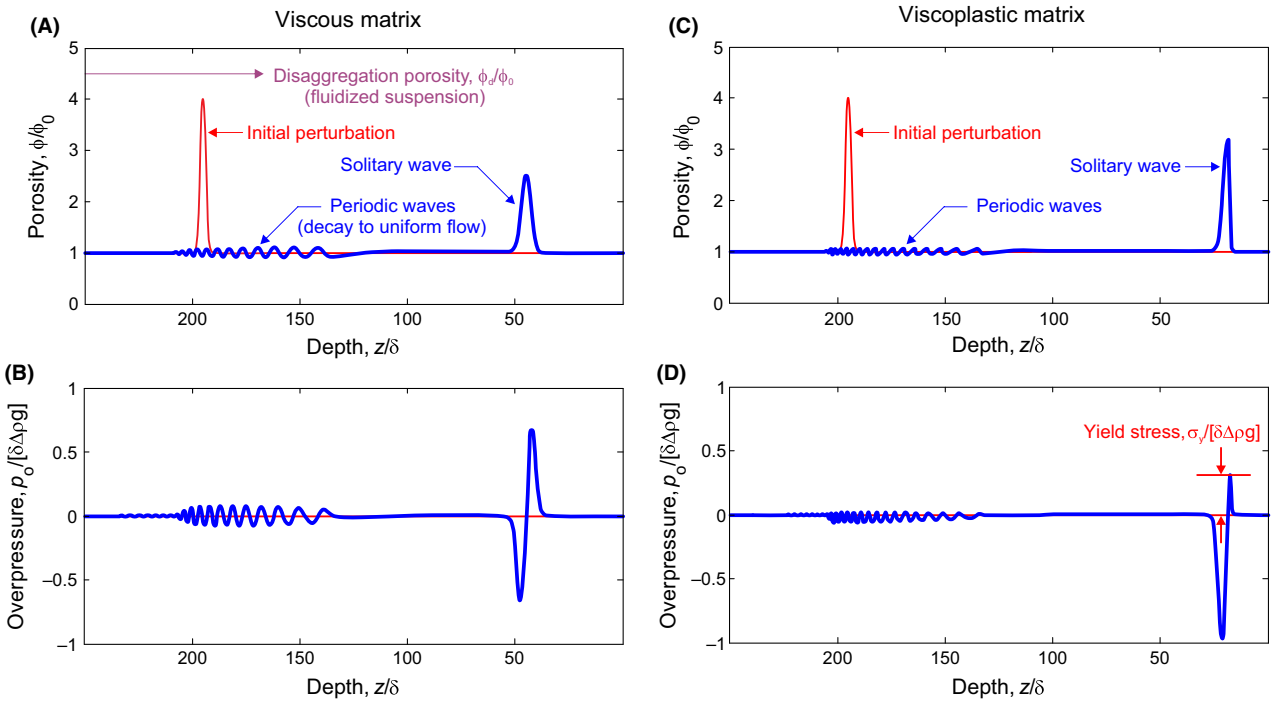

Fig. 1. Numerically simulated porosity wave evolution from a region of increased porosity within an otherwise uniform flow regime through viscous and viscoplastic porous media. (A) Porosity versus depth for the viscous case. The first wave to initiate from the flow perturbation (i.e., the region of elevated porosity) is a solitary wave that propagates above the background porosity in the same direction as fluid flow through the unperturbed matrix. The solitary wave is non-dissipative in the steady-state limit; thus, it propagates infinite distance with essentially unchanging form. Due to transient effects, a periodic wave train initiates behind the solitary wave; the periodic wave train propagates both in and against the direction of fluid flow through the unperturbed matrix. The wave train corresponds to a periodic steady state in which the porosity oscillates about the background level. Porosity wave velocities are proportional to amplitude; thus, with time the solitary wave becomes isolated from the periodic wave train, which has no significant excess volume and degrades to the original uniform flow regime as it spreads. A narrow region of increased porosity was chosen for the initial conditions to emphasize the periodic solution. This choice leads to solitary waves that have lower porosity than the source region. Wider source regions tend to generate waves with porosities that are higher than in the source region; if these porosities exceed the disaggregation porosity (indicated schematically), the matrix disaggregates to a fluidized suspension. This range of porosity wave behavior can also be induced by perturbing the background fluid flux, as might occur as a consequence of devolatilization (melting). (B) Fluid overpressure (negative effective pressure) versus depth for the viscous case, the porosity dependence of the matrix permeability causes fluid pressure anomalies that are responsible for dilating and compacting the porosity during the passage of a wave. Although fluid flow from low to high overpressure may seem to contradict Darcy's law, if the overpressures are converted to hydraulic head, it is apparent that the direction of fluid flow in porosity waves is consistent with Darcy's law. (C) Porosity and (D) overpressure profiles for a viscoplastic scenario in which plasticity is manifest by hydrofracture when overpressure exceeds the brittle yield stress. This rheology affects wave symmetry, but does not fundamentally change porosity wave behavior because the rate of fluid expulsion remains limited by viscous compaction. In the numerical simulation, the effect of the viscoplastic rheology on the periodic waves with overpressures below the yield stress is an artifact of the reduced effective shear viscosity used to simulate brittle failure. Porosity (ϕ), depth (z), overpressure (p_o), and time are scaled relative to the background porosity (ϕ_0), viscous compaction length (δ), characteristic pressure ($\delta|\Delta\rho g|$), and the speed of fluid flow through the unperturbed matrix ($|v_0|$) discussed later in the text. The 1-d volume of the initial perturbation is the same (8.862 $\delta\phi_0$) in both simulations, and the transient profiles (blue curves) are for the same model time (50 $\delta/|v_0|$). The numerical simulations were obtained by finite difference methods for the small porosity formulation (Appendix) with $m_\sigma = 1$, $n_\phi = 3$, and $n_\sigma = 1$.

act as agents for compartmentalization and fluid migration in sedimentary basins (McKenzie 1987; Connolly & Podladchikov 2000; Appold & Nunn 2002) and the lower crust (Suetnova *et al.* 1994; Connolly 1997; Gliko *et al.* 1999; Tian & Ague 2014) are less exotic than seem at first sight. No attempt to make the case for the role of porosity waves in the lower crust is made in this study; rather, the reader is referred to the aforementioned work and recent reviews (Connolly & Podladchikov 2013; Ague 2014) that consider the relevance of the model and the hydraulic properties of the crust in greater detail.

In addition to neglecting 3-d effects, the viscous solitary wave solution neglects the potential roles of plasticity (e.g., brittle failure), elasticity (e.g., fluid compressibility and poroelasticity), and thermal activation. To a first approximation, many of these effects can be inferred from the 1-d viscous model as addressed in the Discussion section of this paper. Elastic effects are the exception. The poroelastic limit, relevant to fluid flow in the upper crust, admits a solitary porosity wave solution that is manifest by fluid pressure surges (Rice 1992). This solitary solution, which is consistent with a variety of upper crustal phenomena (Revil

& Cathles 2002; Miller *et al.* 2004; Joshi *et al.* 2012), contrasts with the viscous case in that it is dissipative and does not require supra-lithostatic fluid pressures. Viscoelastic compaction formulations show that there is a continuum of periodic wave solutions between the viscous and elastic solitary wave limits (Connolly & Podladchikov 1998; Chauveau & Kaminski 2008). However, in numerical simulations, thermal activation of the viscous rheology leads to a rapid variation between a lower crustal regime in which viscoelastic porosity wave solutions show no appreciable elastic character (Connolly 1997) and an upper crustal regime lacking any significant viscous character (Connolly & Podladchikov 1998). These results are taken as justification for the neglect of elastic phenomena in the present treatment of lower crustal fluid expulsion. In this regard, it is important to distinguish fluid expulsion from fluid flow as, particularly in the non-compacting limit, thermoelastic expansivity of the fluid may create pressure gradients responsible for fluid circulation (Hanson 1997; Nabelek 2009; Staude *et al.* 2009).

MATHEMATICAL FORMULATION

Darcyian flow of an incompressible fluid through a viscous matrix composed of incompressible solid grains is considered here largely following the formulation of Scott & Stevenson (1984). Although the solid and fluid components are incompressible, the matrix is compressible because fluid may be expelled from the pore volume. Conservation of solid and fluid mass requires

$$\frac{\partial(1-\phi)}{\partial t}+\nabla\cdot((1-\phi)\mathbf{v}_\mathrm{s})=0 \tag{1}$$

and

$$\frac{\partial\phi}{\partial t}+\nabla\cdot(\phi\mathbf{v}_\mathrm{f})=0, \tag{2}$$

where ϕ is porosity and subscripts f and s distinguish the velocities, $\mathbf{v}$, of the fluid and solid (see Table 1 for notation). From Darcy's law, the force balance between the solid matrix and fluid is

$$\phi(\mathbf{v}_\mathrm{f}-\mathbf{v}_\mathrm{s})=-\frac{k}{\eta_\mathrm{f}}(\nabla p_\mathrm{f}-\rho_\mathrm{f}g\mathbf{u}_z), \tag{3}$$

where k is the hydraulic permeability of the solid matrix, an unspecified function of porosity; ρ_f and η_f are the density and shear viscosity of the fluid, respectively; and $\mathbf{u}_z$ is a downward-directed unit vector. Identifying the mean stress $\bar{\sigma}$ as the vertical load

$$\bar{\sigma}=\int_0^z[(1-\phi)\rho_\mathrm{s}+\phi\rho_\mathrm{f}]\,g\,\mathbf{u}_z\mathrm{d}z. \tag{4}$$

Thus, in terms of the fluid overpressure

$$p_\mathrm{o}=p_\mathrm{f}-\bar{\sigma}, \tag{5}$$

that is, negative effective pressure, Eq. 3 is

$$\phi(\mathbf{v}_\mathrm{f}-\mathbf{v}_\mathrm{s})=-\frac{k}{\eta_\mathrm{f}}(\nabla p_\mathrm{o}+(1-\phi)\Delta\rho g\mathbf{u}_z) \tag{6}$$

where $\Delta\rho=\rho_\mathrm{s}-\rho_\mathrm{f}$. The divergence of the total volumetric flux of matter is the sum of Eqs 1 and 2:

$$\nabla\cdot(\mathbf{v}_\mathrm{s}+\phi(\mathbf{v}_\mathrm{f}-\mathbf{v}_\mathrm{s}))=0, \tag{7}$$

and substituting Eq. 6 into 7 gives

$$\nabla\cdot\left(\mathbf{v}_\mathrm{s}-\frac{k}{\eta_\mathrm{f}}(\nabla p_\mathrm{o}+(1-\phi)\Delta\rho g\mathbf{u}_z)\right)=0. \tag{8}$$

It is assumed that the bulk viscosity of a pure phase is infinite, an assumption necessary to assure that the individual phases do not have time-dependent compressibility (Nye 1953); therefore, viscous compaction must be accomplished by grain-scale shear deformation that eliminates porosity. For solid grains that deform according to a power-law constitutive relation,

$$\dot{\varepsilon}=A|\Delta\sigma|^{n_\sigma-1}\Delta\sigma, \tag{9}$$

where $\dot{\varepsilon}$ is the uniaxial strain rate in response to differential stress $\Delta\sigma$, n_σ is the stress exponent, and A is the coefficient of viscous flow; matrix rheology is then introduced through Terzaghi's effective stress principle as

$$\nabla\cdot v_\mathrm{s}=f_\phi A\left|p_\mathrm{o}^{n_\sigma-1}\right|p_\mathrm{o}, \tag{10}$$

where f_ϕ includes an unspecified porosity dependence and a geometric factor that relates the uniaxial strain rate of the solid to the bulk strain rate of the matrix. In the limit $n_\sigma\to 1$, the shear viscosity of the solid is $\eta_\mathrm{s}=1/(3A)$, and the bulk viscosity of the solid matrix is η_s/f_ϕ. The divergence of the solid velocity is identical to the bulk strain rate of the matrix and related to the compaction rate by

$$\dot{\phi}\equiv-\frac{1}{\phi}\frac{\mathrm{d}\phi}{\mathrm{d}t}=\nabla\cdot v_\mathrm{s}\frac{1-\phi}{\phi}. \tag{11}$$

The power-law form of Eq. 9 precludes certain less common viscous constitutive relations, for example, the exponential form appropriate for low temperature plasticity (Kameyama *et al.* 1999), a completely general derivation, follows if the term $A\left|p_\mathrm{o}^{n_\sigma-1}\right|$ in Eq. 10 is replaced by a generic function of the magnitude of the overpressure.

Equations 1, 8, and 10 form a closed system of equations in the unknown quantities ϕ, p_o, and $\mathbf{v}_\mathrm{s}$. To avoid the unnecessary complication associated with the use of vector notation for a 1-d problem, in the remainder of this analysis vector quantities are represented by signed scalars and the gradient and divergence operators are replaced by $\partial/\partial z$.

Table 1 Frequently used symbols.

Symbol	Meaning
A; A_ϕ	Viscous flow coefficient, Eq. 9; wave amplitude, ϕ_{max}/ϕ_0
a_ϕ	Permeability function geometric factor, Eq. 17
a_σ	Compaction rate function geometric factor, Eq. 19
b_ϕ	Permeability function solidity exponent, Eq. 17
f_ϕ	Compaction rate function, Eq. 19
f_1; f_2	Hydraulic function, Eq. 36; rheological function porosity dependence, Eq. 37
H; ΔH	Hydraulic potential, Eqs 39, 54, 62 and 76; $H(\phi) - H(\phi_0)$
k; k_0	Permeability, Eq. 17; background value
m_σ	Compaction rate function porosity exponent, Eq. 19
n_ϕ	Permeability function porosity exponent, Eq. 17
n_σ	Viscous flow law stress exponent, Eq. 9
p_o; p_f; p	Fluid overpressure, $p_f - p$; fluid pressure; total pressure ($\bar{\sigma}$)
q; q_0	Fluid flux; background value
$\bar{q}_e$; q_s	Time-averaged excess flux, Eq. 61; 1-d fluid production rate
Q	Fluid transport rate for a spherical viscous wave, Eq. 63
Q_p	Fluid transport rate for a 3-d viscoplastic wave, Eq. 65
V_e	1-D wave excess volume, Eq. 60
v_0; v_ϕ	1-D Darcy fluid velocity at $\phi = \phi_0$, $p_o = 0$, Eq. 20; 1-d wave velocity, Eqs 55 and 57
v_ϕ^{crit}	1-D solitary wave critical velocity, Eq. 43
$\mathbf{v}$	3-D velocity
z	Depth coordinate, positive downward
δ	Viscous compaction length scale, Eq. 51
$\Delta\rho$; $\Delta\sigma$	$\rho_s - \rho_f$; differential stress
η_s; η_f	Solid shear viscosity; fluid shear viscosity
λ, λ_p	Viscous wavelength; viscoplastic wavelength
ϕ; ϕ_0; ϕ_d	Hydraulically connected porosity; background value; value at disaggregation
ϕ_1; ϕ_{max}	Focal point porosity, a real root of $f_1 = 0$; maximum wave porosity
ρ_s; ρ_f	Solid density; fluid density
$\bar{\sigma}$; σ_y	Mean stress (p); failure stress
τ	Compaction timescale, $\delta/\lvert v_0\rvert$
∇, $\nabla\cdot$	Gradient, divergence
$f\lvert_{x=x_0}$	Value of a function f at $x = x_0$

The 1-d steady state

For analytical purposes, the existence of a 1-d solitary porosity wave solution is assumed in which the wave propagates with unchanging form and velocity through a matrix with an initial fluid-filled porosity ϕ_0 at zero overpressure. In a reference frame that travels with the wave, integration of Eq. 1 gives the solid velocity as

$$v_s = v_\infty \frac{1-\phi_0}{1-\phi} \tag{12}$$

where $v_\infty(1-\phi_0)$ is the solid flux at infinite distance from the wave. After substitution of Eq. 12, the integrated form of Eq. 8 can be rearranged to

$$\frac{\partial p_o}{\partial z} = \left(q_t - v_\infty \frac{1-\phi_0}{1-\phi}\right)\frac{\eta_f}{k} - (1-\phi)\Delta\rho g \tag{13}$$

where $q_t = \phi v_f + (1-\phi)v_s$ is the constant, total, volumetric flux of matter through the column, which evaluates in the limit $\phi \to \phi_0$ and $p_o \to 0$ as

$$q_t = v_\infty - (1-\phi_0)\frac{k_0}{\eta_f}\Delta\rho g \tag{14}$$

where k_0 is the permeability at ϕ_0. Making use of Eq. 14, Eq. 13 is rewritten

$$\frac{\partial p_o}{\partial z} = v_\infty \frac{\eta_f}{k}\frac{\phi-\phi_0}{1-\phi} - \Delta\rho g\left(1-\phi-(1-\phi_0)\frac{k_0}{k}\right). \tag{15}$$

Likewise, after substitution of Eq. 12, Eq. 10 can be rearranged to

$$\frac{\partial \phi}{\partial z} = \frac{(1-\phi)^2}{1-\phi_0}\frac{f_\phi}{v_\infty} A|p_o|^{n_\sigma - 1} p_o. \tag{16}$$

For a given wave velocity, Eqs 15 and 16 form a closed system of two partial differential equations in two unknown functions (ϕ and p_o) of depth.

Constitutive relations and scales

Although general forms are retained where possible, to place the analysis in context it is useful to specify possible constitutive relations for permeability and the porosity dependence, f_ϕ, of the rheological constitutive relation (Eq. 10). To describe the variation in permeability due to compaction, the theoretical Carman–Kozeny porosity–permeability relationship (Carman 1939) is generalized as

$$k = a_\phi \frac{\phi^{n_\phi}}{(1-\phi)^{b_\phi}} \tag{17}$$

where a_ϕ is a grain-size-dependent material constant and the formal values of b_ϕ and n_ϕ, 2 and 3, respectively, imply that the first-order control on the porosity dependence of the permeability at small porosity is determined by n_ϕ. From analysis of in situ rock permeability, Neuzil (1994) shows that pore geometry and grain size gives rise to variations in permeability that span eight orders of magnitude, but that porosity dependence is approximately cubic. A cubic dependence is predicted from theory irrespective of whether flow is intergranular or fracture controlled (Norton & Knapp 1977; Gavrilenko & Gueguen 1993). Accordingly, a cubic dependence, that is, $n_\phi = 3$, is considered to be most relevant. Higher exponents are observed in rocks where the degree of hydraulic connectivity varies strongly with porosity (Zhu *et al.* 1995, 1999). The solidity (i.e., $1-\phi$) exponent b_ϕ is constrained by considering the settling of a single grain through a static fluid. In this case, both the effective pressure and its gradient vanish, and substitution of Eq. 17 into Eq. 6 yields the settling velocity

$$v_s = \frac{a_\phi}{\eta_f}\frac{\phi^{n_\phi - 1}}{(1-\phi)^{b_\phi - 1}}\Delta\rho g, \tag{18}$$

which is an increasing function for all allowed values of porosity only if $1 \le b_\phi < n_\phi$ and finite at $\phi \to 1$, as required by Stoke's law, only if $b_\phi = 1$.

The porosity dependence f_ϕ of the rheological equation (Eq. 10) must satisfy two physical constraints. In the limit $\phi \to 0$, f_ϕ must likewise vanish so that effective bulk viscosity becomes infinite to assure that the pure solid does not compact; and in the limit $\phi \to \phi_d$, f_ϕ must be infinite to assure that the solid and fluid pressure fields converge when the matrix has no cohesive strength, that is, when the matrix is fluidized. In detail, this transition is likely to be complex and material dependent, but theoretical and experimental considerations suggest that the transition occurs at $\phi_d \sim 20\%$ (Arzi 1978; Auer *et al.* 1981; Ashby 1988; Vigneresse *et al.* 1996). To account for these limits, the expressions of Wilkinson & Ashby (1975), derived explicitly for compaction by dislocation creep, are generalized here as:

$$f_\phi = a_\sigma \phi^{m_\sigma}(1-\phi)/\left(1-\phi^{1/n_\sigma}\right)^{n_\sigma}(\phi_d/|\phi_d-\phi|)^{n_\sigma-1/2} \quad (19)$$

where formally $m_\sigma = 1$ and, for spherical pores, $a_\sigma = n_\sigma^{-n_\sigma}(3/2)^{n_\sigma+1}$. For diffusion-controlled compaction, a_σ is strongly dependent on grain size and the exponent m_σ varies between 1/2 and 5/6 (Ashby 1988). In practice, the numerous compaction formulations in the geological literature differ primarily in the choice of m_σ. For simplicity, early studies neglected the porosity dependence ($m_\sigma = 0$; McKenzie 1984; Barcilon & Richter 1986), whereas most recent formulations (Sumita *et al.* 1996; Connolly 1997; Bercovici *et al.* 2001) take $m_\sigma = 1$.

Many of the material properties relevant to geological compaction vary over orders of magnitude and/or are extraordinarily uncertain (Neuzil 2003); for this reason, no attempt is made to parameterize the relations used here. Rather, results are given relative to the background porosity, Darcyian fluid velocity through the unperturbed matrix

$$v_0 = \frac{k_0}{\eta_f \phi_0}(1-\phi_0)\Delta\rho g, \quad (20)$$

or its speed $c_0 = |v_0|$, and the compaction length scale

$$\delta = \sqrt[n_\sigma+1]{\left(\frac{2}{3}\right)^{n_\sigma+1}\frac{k_0 n_\sigma^{n_\sigma}}{A\eta_f \phi_0^{m_\sigma}}|\Delta\rho g|^{1-n_\sigma}} \quad (21)$$

suggested by non-dimensionalization of Eqs 15, 16 and 19 in the small porosity limit (Appendix), a limit that has the consequence that the solutions are independent of the absolute porosity. The scales for pressure, time, and fluid flux are then $p_0 = \delta|\Delta\rho g|$, $\tau = \delta/|v_0|$, and $q_0 = \phi_0 v_0$, respectively. Parameter ranges relevant to lower crustal fluid flow are reviewed elsewhere (Connolly & Podladchikov 2013; Ague 2014).

For a linear-viscous matrix with shear viscosity $\eta_s = 1/(3A)$, Eq. 21 simplifies to

$$\delta = \sqrt{\frac{4}{3}\frac{\eta_s}{\phi_0^{m_\sigma}}\frac{k_0}{\eta_f}}, \quad (22)$$

which, accounting for differences in the formulation of the bulk viscosity of the matrix, is identical to the viscous compaction length of McKenzie (1984). In the linear viscous case with $m_\sigma = 1$, δ is the length scale over which the bulk strain rate would change by a factor of e, the base of the natural logarithm, for the characteristic overpressure gradient $\Delta\rho g$. It is therefore the length scale over which compaction processes would generate an e-fold variation in porosity. For the present formulation, the analytical significance of δ is less clear, but it emerges that δ remains a reasonable estimate of the length scale for an e-fold variation in porosity.

ANALYTICAL SOLUTION FOR THE 1-D STEADY STATE

The steady-state wave solutions to the compaction Eqs 13 and 16 are best understood by analogy with the solutions to the equations of motion of an initially stationary ball on a frictionless 1-d curved surface in response to gravitational acceleration. To exploit this analogy, the solution for an oscillating ball (Fig. 2) is recapitulated here.

The oscillating ball

The equations of motion for the ball are its acceleration due to gravity

$$\frac{\partial v}{\partial t} = -\frac{\partial h}{\partial x}g \quad (23)$$

and the definition of velocity

$$\frac{\partial x}{\partial t} = v \quad (24)$$

where x is the horizontal position of the ball, v is its velocity, and h is a shape function that describes the height of the surface as a function of x. Combining Eqs 23 and 24 to eliminate time

$$\frac{\partial v}{\partial x} = -\frac{g}{v}\frac{\partial h}{\partial x} \quad (25)$$

and rearranging Eq. 25 yields

$$0 = v\mathrm{d}v + g\frac{\partial h}{\partial x}\mathrm{d}x. \quad (26)$$

The indefinite integral of Eq. 26 defines a property

$$u \equiv \frac{v^2}{2} + gh, \quad (27)$$

the energy per unit mass, which is conserved by the ball. The solutions to Eqs 23 and 24 correspond to contours of u as a function of v and x, where, through Eq. 27 at $v = 0$, the initial height of the ball (Fig. 2A) defines the

contour of interest for a particular problem (Fig. 2B). Closed contours (e.g., the red contour in Fig. 2B) correspond to a wave solution in which the ball oscillates between its initial position, x_i, and a position of equal height at which its kinetic energy vanishes, and open contours (e.g., the blue contour in Fig. 2B) correspond to an aperiodic (i.e., non-wave) solution in which the ball rolls indefinitely away from its initial position. Because u is a monotonic function of v and is directly proportional to h, the focus of any closed contour must lie along the $v = 0$ axis and correspond to an extremum in h, that is, a real root of $\partial h/\partial x = 0$. From physical considerations, it is evident that the solution is only stable if this root is a minimum, that is, $\partial^2 h/\partial x^2 > 0$. A well-known implication of this solution is that shape function h entirely determines both the amplitude and stability of oscillation, while the gravitational constant controls the velocity of the ball and therefore the period of oscillation.

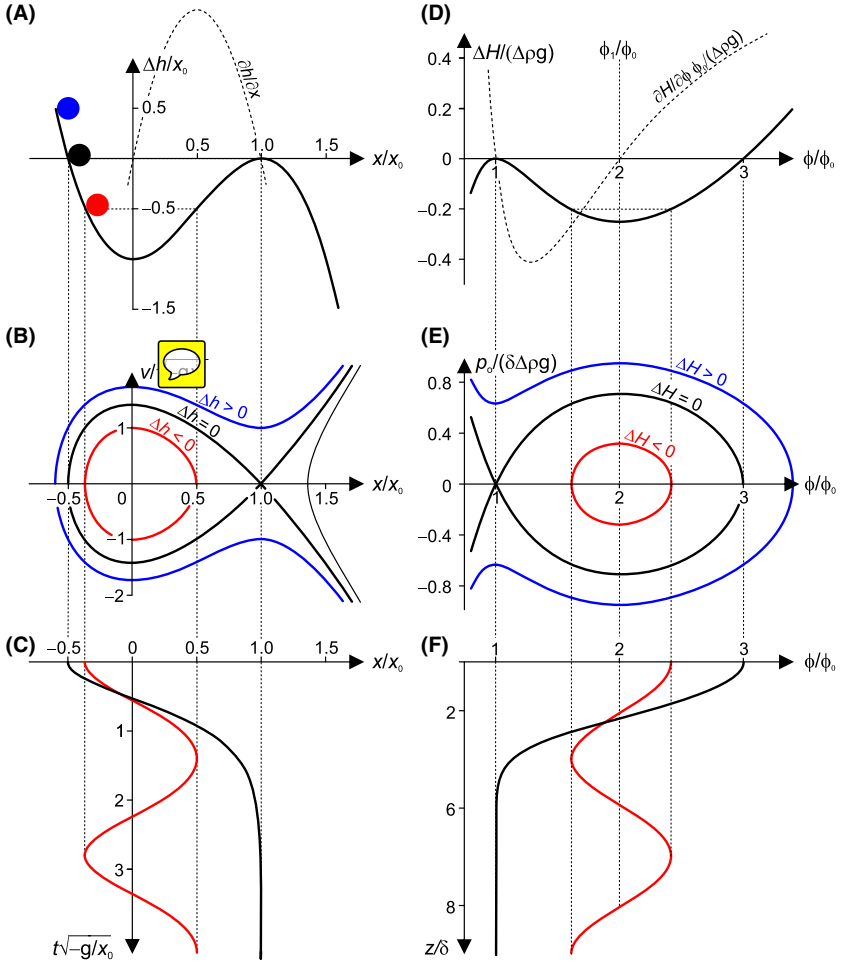

Fig. 2. Analogy of porosity waves with the oscillatory movement of a ball on a frictionless surface of variable height with a local maximum (i.e., a saddle point). In the analogy, the porosity wave properties H, ϕ, p_o, and z map to h, x, v, and t of the oscillating ball. If the ball is placed on the surface (e.g., the red ball in A) at a height below and to the left of the local maximum, the ball oscillates between points of equal height. In this case, the velocity-position trajectory of the ball defines a closed path around the focal point at $x = v = 0$ (e.g., the red curve in B) and its velocity-time (or position-time) trajectory defines a periodic wave train (e.g., the red curve in C). The location of the focal point ($x/x_0 = 0$) for the waves is dependent only on the shape of the surface, whereas the wave frequency is controlled by the gravitational acceleration. The solitary wave solution for the oscillating ball corresponds to the case that a ball (i.e., the black ball in A) is placed on the surface at the height of the saddle point. In this case, the ball would have no kinetic energy if it reached the saddle point; however, because the ball decelerates as it approaches the saddle point, the wave solution has an infinite period. If the ball is released from a height above the saddle point (i.e., the blue ball in A), it rolls continuously away from its initial position and there is no wave solution to the governing equations. The analogy of the oscillating ball to porosity wave solution is imperfect only in that the shape of function, or hydraulic potential, H of the porosity wave is dependent on wave velocity (Fig. 3), which is related to the intensity of the perturbation responsible for generating waves. For the velocity specified for H as illustrated in (D), the only wave solution capable of stably connecting the background porosity to a region of increased porosity is the solitary wave (i.e., the black trajectories in E and F); the periodic solutions (e.g., the red trajectories E and F) correspond to waves in which the porosity would oscillate about the focal point ($\phi/\phi_0 = 2$) between a porosity that is less than the maximum porosity of the solitary wave and greater than the background porosity. The solitary wave shape function illustrated in (D) is from the small porosity formulation of the compaction equations (Appendix) with $m_\sigma = 0$, $n_\phi = 3$, and $v_\phi/v_0 = 7$.

For a ball placed at position x_i with $v_i = 0$, its velocity as it accelerates from its initial position can be computed by rearranging the definite integral of Eq. 26 as

$$v = \sqrt{-2g\Delta h} \tag{28}$$

where $\Delta h = h - h_i$ and h_i is height of the ball at x_i. The time dependence of the solution is then recovered by substitution of Eq. 28 into Eq. 24 and inverting the result to obtain

$$t = \frac{1}{\sqrt{2g}} \int_{x_i}^{x} \frac{dx}{\sqrt{\Delta h}}, \tag{29}$$

For oscillatory solutions, Eq. 29 gives the time dependence of the solution for half the period of the oscillation. Thus, the oscillatory solution corresponds to a periodic wave (e.g., the red curve in Fig. 2C) in position (or velocity) as a function of time.

To quantify the preceding discussion, consider an arbitrarily chosen shape function such that

$$\frac{\partial h}{\partial x} = \frac{6}{x_0^2} x(x_0 - x), \tag{30}$$

which integrates to $h = x^2(3x_0 - 2x)/x_0^2$. The roots of Eq. 30 define the local extrema of h; thus, the surface has extrema at the structural root $x = 0$, at which $h = 0$, and the general root $x = x_0$, at which $h = h_0 = x_0$. Restricting attention to the case $x_0 < 0$, for which the general root is a maximum, the structural root $x = 0$ is the focus of all possible wave solutions and the general root x_0 defines the maximum value of x_i for which these solutions are possible (Fig. 2A). The minimum value of x_i, that is, $-x_0/2$, at which a wave solution is possible is obtained by solving $h = h_0$ for $x_i < x_0$. The closed contour of u as a function of position and velocity that demarcates the boundary between periodic and aperiodic solutions corresponds to a solitary solution. The existence of such a solution requires that h has at least two extrema. In the present example, the solution corresponds to portion of the contour of u that emanates from the saddle point located by the structural root x_0 at $v = 0$ (the black contour in Fig. 2B at $x/x_0 < 1$). In distinction to the periodic solutions, for the solitary wave solution, after the ball is released it does not return to its initial position, but rather comes to rest at the saddle point (at $x/x_0 = 1$), where its height is identical to its initial height. The physical reason for this behavior is that both the acceleration on the ball and its kinetic energy vanish at the saddle point. This trajectory (the black curve in Fig. 2C) is half the solitary wave solution; the complete solution would be obtained if the motion of the ball initiated from the saddle point. The absence of both kinetic energy and acceleration at the saddle point strictly precludes the occurrence of the complete solitary solution; however, the negative curvature of the surface at the saddle point has the consequence that a ball placed at the saddle point would be unstable with respect to infinitesimally small perturbations.

There are two types of solitary solution distinguished on the basis of whether the period of the solution is finite or infinite. The origin of these solutions can be understood by a thought experiment in which the initial conditions are chosen to coincide exactly with the conditions at which the trajectory of the solitary solution crosses the $v = 0$ axis, that is, in the present example at $x/x_0 = -1/2$ (Fig. 2A). As the ball has no kinetic energy and is at height $h = h_0$, the ball has exactly the energy necessary to reach the saddle point x_0, but because the acceleration of the ball becomes vanishingly small as the saddle point is approached, the time required for the ball to reach the saddle point may be infinite. In the present example, it can be verified by analytic integration of Eq. 29 that the time required for the ball to reach the saddle point is infinite; this result can be deduced more generally by observing that it is only necessary to consider the motion of the ball in the immediate vicinity of the saddle point. Accordingly, taking the first non-zero term of a Taylor series expansion of Eq. 28 about x_0

$$v \approx \pm \sqrt{-g \left.\frac{\partial^2 h}{\partial x^2}\right|_{x=x_0}}. \tag{31}$$

Equation 29 then evaluates as

$$t \approx \frac{\ln(X)}{\sqrt{-g \left.\frac{\partial^2 h}{\partial x^2}\right|_{x=x_0}}} \tag{32}$$

where $X = x - x_0$ is the distance from the saddle point and noting that $\left.\partial^2 h/\partial x^2\right|_{x=x_0} < 0$ is a necessary condition for x_0 to be a saddle point, it follows that $t \to \infty$ as $X \to 0$. Thus, solitary solutions to Eqs 23 and 24 are of infinite period regardless of the details of the shape function. Rearranging Eq. 32 to express the distance of the ball from the saddle point as a function of time

$$X \approx e^{t/\tau} \tag{33}$$

where $\tau = 1/\sqrt{-g\left.\partial^2 h/\partial x^2\right|_{x=x_0}}$ provides a natural timescale for the motion of the ball.

Wave solutions to the compaction equations

To make the analogy between the wave solutions of the compaction equations and the oscillating ball apparent, Eqs 15 and 16 are abbreviated as

$$\frac{\partial p_o}{\partial z} = f_1 \tag{34}$$

and

$$\frac{\partial \phi}{\partial z} = f_2 \frac{A}{v_\phi} |p_o|^{n_\sigma - 1} p_o \tag{35}$$

where $v_\phi = -v_\infty$ is the velocity of a wave relative to a fixed point in the unperturbed matrix and f_1 and f_2 are

$$f_1 = -v_\phi \frac{\eta_f}{k} \frac{\phi - \phi_0}{1 - \phi} - \Delta\rho g \left[1 - \phi - (1 - \phi_0) \frac{k_0}{k} \right] \tag{36}$$

and

$$f_2 = \frac{(1 - \phi)^2}{1 - \phi_0} f_\phi. \tag{37}$$

Combining Eqs 34 and 35 to eliminate z, and rearranging, yields

$$0 = |p_o|^{n_\sigma - 1} p_o \mathrm{d}p_o - \frac{v_\phi f_1}{A f_2} \mathrm{d}\phi, \tag{38}$$

which must be satisfied by the $\phi - p_o$ trajectory of any steady-state solution to Eqs 15 and 16. Defining a function H such that

$$H \equiv -\int \frac{f_1}{f_2} \mathrm{d}\phi. \tag{39}$$

or $\partial H / \partial \phi = -f_1 / f_2$, Eq. 38 is rewritten as

$$0 = |p_o|^{n_\sigma - 1} p_o \mathrm{d}p_o + \frac{v_\phi}{A} \frac{\partial H}{\partial \phi} \mathrm{d}\phi. \tag{40}$$

Comparison of Eqs 40 and 26 reveals that wave solutions to the compaction equations, at constant phase velocity, are a mathematical analog to the equations of motion for the oscillating ball, wherein the compaction variables $[\phi, p_o, z]$ map to $[x, v, t]$; the shape function H can be thought of as a hydromechanical potential that corresponds to the height h of the ball, and the factor v_ϕ / A has the same role as the gravitational constant g. Integration of Eq. 40 defines a property

$$U \equiv \frac{|p_o|^{n_\sigma - 1} p_o^2}{n_\sigma + 1} + \frac{v_\phi}{A} H \tag{41}$$

akin to the mass normalized energy u for the oscillating ball, which is conserved by porosity waves. Closed contours of U define the wave solutions to the compaction equations as a function of p_o and ϕ for a given velocity. As in the case of the oscillating ball, closed contours define periodic solutions where the porosity oscillates between two values, characterized by equal H, at which p_o vanishes (e.g., the red contour in Fig. 2E). The periodic solutions are bounded by the contour that defines the solitary solution (black contour, Fig. 2E). Likewise analogous to the oscillating ball solution, because U is directly proportional to H and increases with both negative and positive overpressure, the focus of any closed contour must lie along the $p_o = 0$ axis and correspond to an extremum in H, for example, the real root, ϕ_1, of $\partial H / \partial \phi = 0$. The porosity dependence (f_2) of the rheologic equation (Eq. 35) must be finite and positive if the matrix is coherent; consequently, the roots of $\partial H / \partial \varphi = 0$ are independent of the rheologic constitutive relationship and identical to the roots of the hydraulic equation (Eq. 34), that is, the porosities that satisfy $f_1 = 0$. Although the number of roots cannot be determined without specifying the porosity–permeability relationship, the formulation of Eq. 15 is such that ϕ_0 is always a root, analogous to x_0 in Eq. 30. Consequently, if

$$\left. \frac{\partial^2 H}{\partial \phi^2} \right|_{\phi = \phi_0} = \frac{\Delta\rho g}{f_2|_{\phi = \phi_0}} \left(\frac{1 - \phi_0}{k_0} \left. \frac{\partial k}{\partial \phi} \right|_{\phi = \phi_0} - 1 + \frac{v_\phi}{\phi_0 v_0} \right) \tag{42}$$

is greater than zero, then ϕ_0 is a stable level of porosity and small flow perturbations to a uniform flow regime will lead to periodic oscillations in the porosity about ϕ_0 (Fig. 3A). In contrast, if H is a maximum at ϕ_0, then ϕ_0 is a saddle point and solitary wave solutions are possible (Fig. 3B). Equating Eq. 42 to zero and solving for v_ϕ yields the critical velocity at which the background porosity ϕ_0 switches from focal to saddle point

$$v_\phi^{\mathrm{crit}} = v_0 \phi_0 \left(1 - \frac{(1 - \phi_0)}{k_0} \left. \frac{\partial k}{\partial \phi} \right|_{\phi = \phi_0} \right) \tag{43}$$

such that ϕ_0 is a saddle point for waves with $v_\phi / v_0 > v_\phi^{\mathrm{crit}} / v_0$, which is thus a necessary condition for the existence of the solitary wave solution. Although Eq. 43 appears to admit the possibility of solitary waves that propagate against the direction of buoyancy-driven fluid flow through the unperturbed matrix, substituting the explicit function for permeability given by Eq. 17 in Eq. 43 yields

$$v_\phi^{\mathrm{crit}} / v_0 = \left[n_\phi (1 - \phi_0) + \left(b_\phi - 1 \right) \phi_0 \right], \tag{44}$$

which is positive for any plausible choice of n_ϕ and b_ϕ, as discussed earlier.

Provided a solitary wave solution exists, that is, $v_\phi / v_0 > v_\phi^{\mathrm{crit}} / v_0$ and $H(\phi_d) > H(\phi_0)$ (as in Fig. 3B), then solving $\Delta H = H(\phi) - H(\phi_0) = 0$ yields the maximum porosity of the wave $\phi_{\max}$. As the overpressure vanishes at $\phi_{\max}$, the dependences of p_o and z on ϕ are obtained in exactly the same manner as the dependence of v and t on x for the oscillating ball (Eqs 28 and 29). Thus, from the definite integral of Eq. 40

$$p_o = \pm \sqrt[n_\sigma + 1]{(n_\sigma - 1) \frac{v_\phi}{A} \Delta H} \tag{45}$$

and inverting the result of substitution of Eq. 45 into Eq. 35,

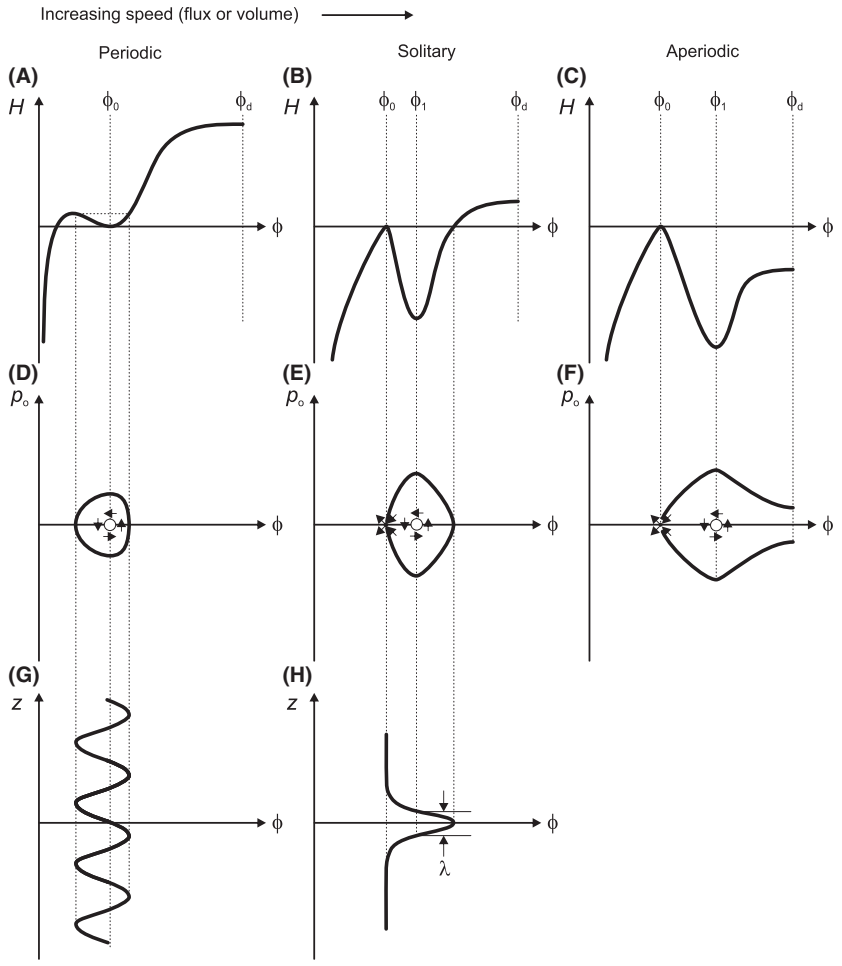

Fig. 3. Shape functions, phase portraits, and porosity wave patterns as a function of phase velocity illustrating the periodic, solitary, and aperiodic (fluidized) compaction-driven flow regimes. In general, phase velocity can be taken as a measure of the intensity of a flow perturbation. At low velocities (A, D, G), the background porosity ϕ_0 is the focal point of a periodic solution. At intermediate velocities (B, E, H), the focal point, that is, the minimum in H, shifts to $\phi_1 > \phi_0$; the potential H recovers to $H(\phi_0)$ at a porosity intermediate between ϕ_1 and the disaggregation porosity ϕ_d; and the relevant solution is a solitary wave. At still higher velocities (C, F), $H(\phi_d) < H(\phi_0)$ so there is no steady-state wave solution as there is no closed path in $p_o - \phi$ space connecting ϕ_0 to an elevated level of porosity; and the perturbation causes the matrix to disaggregate.

$$z = \pm \sqrt[n_\sigma+1]{\frac{v_\phi}{A}} \int_{\phi_{max}}^{\phi} \frac{d\phi}{p_o^{n_\sigma} f_2}, \tag{46}$$

where z is the depth relative to the wave center at which $\phi = \phi_{max}$ and $p_o = 0$. Any porosity of the solitary solution is associated with both positive and negative values of p_o and z, corresponding to the upper and lower halves of the wave. For this reason, the sign of factors in expressions for p_o and z has no significance; rather than explicitly indicating this with magnitude notation in Eqs 45 and 46, and subsequent equations, it is to be understood that any negative term is to be replaced by its absolute value.

Nonlinear rheology creates a distinction between the solitary solution of the compaction equations and that of the oscillating ball in that it is possible to obtain a solitary porosity wave of finite wavelength. This behavior is demonstrated by linearizing Eq. 46 about ϕ_0 to obtain

$$z \approx \pm \left(\frac{v_\phi}{A f_2|_{\phi=\phi_0}} \left(\frac{n_\sigma + 1}{2} \frac{\partial f_1}{\partial \phi}\bigg|_{\phi=\phi_0} \right)^{-n_\sigma} \right)^{\frac{1}{n_\sigma+1}} \int_{\Phi}^{0} \Phi^{-\frac{2n_\sigma}{n_\sigma+1}} d\Phi, \tag{47}$$

where $\Phi = \phi - \phi_0$. The bifurcation between finite- and infinite-wavelength solutions is determined entirely by the stress exponent in Eq. 47, such that finite solutions can exist only for $n_\sigma < 1$, and is independent of the details of the hydraulic potential. As $n_\sigma \geq 1$ is characteristic of viscous behavior in rocks, it is expected that solitary porosity waves only develop in viscous rocks with finite initial porosity. Finite-wavelength solitary waves propagate, by definition, through a matrix with no initial porosity. It has been shown elsewhere that finite-wavelength solutions exist for viscoelastic compaction rheology (Connolly & Podladchikov 1998); the present analysis raises the possibility that shear thickening viscous mechanisms ($n_\sigma < 1$) could also operate at the zero porosity limit in natural systems.

Just as the linearized equation for time in the oscillating ball problem (Eq. 33) provides a natural timescale for the movement of the ball near x_0, the linearized equation for

depth in the solution of the compaction equations provides a characteristic length scale for variations in porosity near ϕ_0. By rewriting the integral in Eq. 47 in terms of $d\ln\Phi$, and differentiating, this length scale is

$$\delta' \sim \frac{\partial z}{\partial \ln \Phi} \approx \left(\Phi^{1-n_\sigma} \frac{v_\phi}{A f_2|_{\phi=\phi_0}} \left(\frac{n_\sigma + 1}{2} \frac{\partial f_1}{\partial \phi}\Big|_{\phi=\phi_0} \right)^{-n_\sigma} \right)^{\frac{1}{n_\sigma+1}}, \tag{48}$$

the depth interval over which porosity decays from $e\phi_0$ to ϕ_0 within a solitary wave. The derivative on the right-hand side of Eq. 48

$$\frac{\partial f_1}{\partial \phi}\Big|_{\phi=\phi_0} = \frac{\Delta\rho g}{\phi_0} \left(\frac{v_\phi^{\text{crit}}}{v_0} - \frac{v_\phi}{v_0} \right) \approx -\frac{\Delta\rho g}{\phi_0} \frac{v_\phi}{v_0} \tag{49}$$

is zero at $v_\phi = v_\phi^{\text{crit}}$, but decreases monotonically in v_ϕ; thus, the approximate form is valid for large speeds. Adopting this approximation, substituting $\Phi = (e - 1)\,\phi_0$ in Eq. 48, and expanding f_2 at ϕ_0 as $a_\sigma f_\phi|_{\phi=\phi_0}(1 - \phi_0)$ yields

$$\delta' \sim \frac{\partial z}{\partial \ln \Phi} \approx \left(\frac{v_\phi [\phi_0 (e-1)]^{1-n_\sigma}}{A a_\sigma f_\phi|_{\phi=\phi_0} (1-\phi_0)} \left[\frac{n_\sigma + 1}{2} \frac{\Delta\rho g}{\phi_0} \frac{v_\phi}{v_0} \right]^{-n_\sigma} \right)^{\frac{1}{n_\sigma+1}}, \tag{50}$$

effectively a lower bound on the wavelength of the solitary solution. Making use of the constitutive relations and scales given by Eqs 17, 19 and 20, and estimating wave speed as the magnitude of v_ϕ^{crit} ($\sim n_\phi |v_0|$, Eq. 44), then in the small porosity limit

$$\delta' = \frac{\sqrt[n_\sigma+1]{n_\sigma^{n_\sigma} \left(\frac{2}{3}\right)^{n_\sigma+1} \frac{a_\phi \phi_0^{n_\sigma - m_\sigma}}{A\eta_f} |\Delta\rho g|^{1-n_\sigma}}}{\sqrt[n_\sigma+1]{\left(\frac{2}{n_\sigma+1}\right)^{n_\sigma} \left(n_\phi [e-1]\right)^{1-n_\sigma}}}, \tag{51}$$

where the first factor is the scale δ obtained by dimensional analysis (Eq. 21) and the second factor is unity for the linear viscous case and close to, but less than, one for the nonlinear case with typical values of n_ϕ and n_σ. This result confirms that δ is a reasonable estimate of the compaction length scale and suggests, unsurprisingly, that increasing the nonlinear character of the viscous rheology generally leads to stronger spatial variations in porosity. In view of the minor difference between δ and δ', δ is preferred here because of its simplicity.

Solitary wave properties in the small porosity limit

To illustrate features of the solitary waves explicitly, the solution is considered in conjunction with the constitutive relations given by Eqs 17 and 19 in the small porosity limit ($1 - \phi \to 1$, $\phi_d - \phi \to \phi_d$). Eqs 34 and 35 are then

$$\frac{\partial p_o}{\partial z} = \Delta\rho g \left(\frac{v_\phi}{v_0} \frac{[(\phi/\phi_0) - 1] + 1}{[\phi/\phi_0]^{n_\phi}} - 1 \right) \tag{52}$$

and

$$\frac{\partial \phi}{\partial z} = A a_\sigma \frac{\phi^{m_\sigma}}{v_\phi} |p_o|^{n_\sigma - 1} p_o, \tag{53}$$

respectively. Making use of these forms, the wave hydraulic potential H can be arranged as the sum of two integrals

$$H = \frac{\Delta\rho g}{\phi_0^{m_\sigma} a_\sigma} \int \left(\frac{\phi_0}{\phi}\right)^{m_\sigma} - \left(\frac{\phi_0}{\phi}\right)^{n_\phi + m_\sigma} d\phi + \frac{\Delta\rho g}{\phi_0^{m_\sigma} a_\sigma} \frac{v_\phi}{v_0} \int \left(\frac{\phi_0}{\phi}\right)^{n_\phi + m_\sigma} - \left(\frac{\phi_0}{\phi}\right)^{n_\phi + m_\sigma - 1} d\phi \tag{54}$$

where both integrands are zero at $\phi = \phi_0$, and for $\phi > \phi_0$, $n_\phi > 1$, and $m_\sigma \geq 0$, the first integrand is positive and the second integrand negative. Further, for conditions at which the solitary solution is possible, that is, $v_\phi/v_0 > v_\phi^{\text{crit}}/v_0$, H is a maximum at $\phi = \phi_0$, and H must have a minimum at the ϕ_1, the focal point where $\partial p_o/\partial z$ (Eq. 52) vanishes and the magnitude of the overpressure is a maximum (Fig. 3B). At $\phi > \phi_1$, H recovers to the background value $H(\phi_0)$ at the maximum porosity of the wave $\phi_{\max}$. It follows from the form of Eq. 54 that for a fixed choice of exponents, the rate at which H recovers to the background value $H(\phi_0)$ at $\phi > \phi_1$ decreases with wave speed. Thus, wave amplitude must increase with wave speed (Fig. 4A). For specified v_ϕ, the leading term of the first integrand will dominate the rate at which H recovers to $H(\phi_0)$ at $\phi > \phi_1$. Consequently, increasing m_σ increases amplitude (cf. solid black and cyan curves, Fig. 4A); this result is intuitive because increasing the nonlinearity of the effective bulk viscosity leads to a weakening of the matrix with increasing porosity. A less intuitive consequence of Eq. 54 is that increasing the nonlinearity of the porosity–permeability relationship, that is, increasing n_ϕ, decreases wave amplitude (cf. orange and black curves, Fig. 4A). This occurs because at $\phi > \phi_1$ the rate at which the sum of the integrands decays with porosity increases with n_ϕ.

The relationship between wave velocity and amplitude ($A_\phi = \phi_{\max}/\phi_0$) for $m_\sigma \neq 1$ obtained by solving $\Delta H = 0$ is

$$v_\phi = v_0 \frac{n_\phi + m_\sigma - 2}{1 - m_\sigma} \frac{\left([m_\sigma - 1] \left[A_\phi^{-n_\phi} - 1 \right] - n_\phi \right) A_\phi^{1-m_\sigma} + n_\phi}{A_\phi^{1-n_\phi-m_\sigma} \left([n_\phi + m_\sigma - 1][A_\phi - 1] + 1 \right) - 1}, \tag{55}$$

which for the specific case $n_\phi = 3$ and $m_\sigma = 0$ reduces to the linear relationship $v_\phi = v_0(2A_\phi + 1)$ obtained by Scott & Stevenson (1984, Barcilon & Richter 1986). The integrated form of Eq. 53 for general values of m_σ is singular at $m_\sigma = 1$, the value typically assumed in compaction literature. For this less general, but more widely used, case

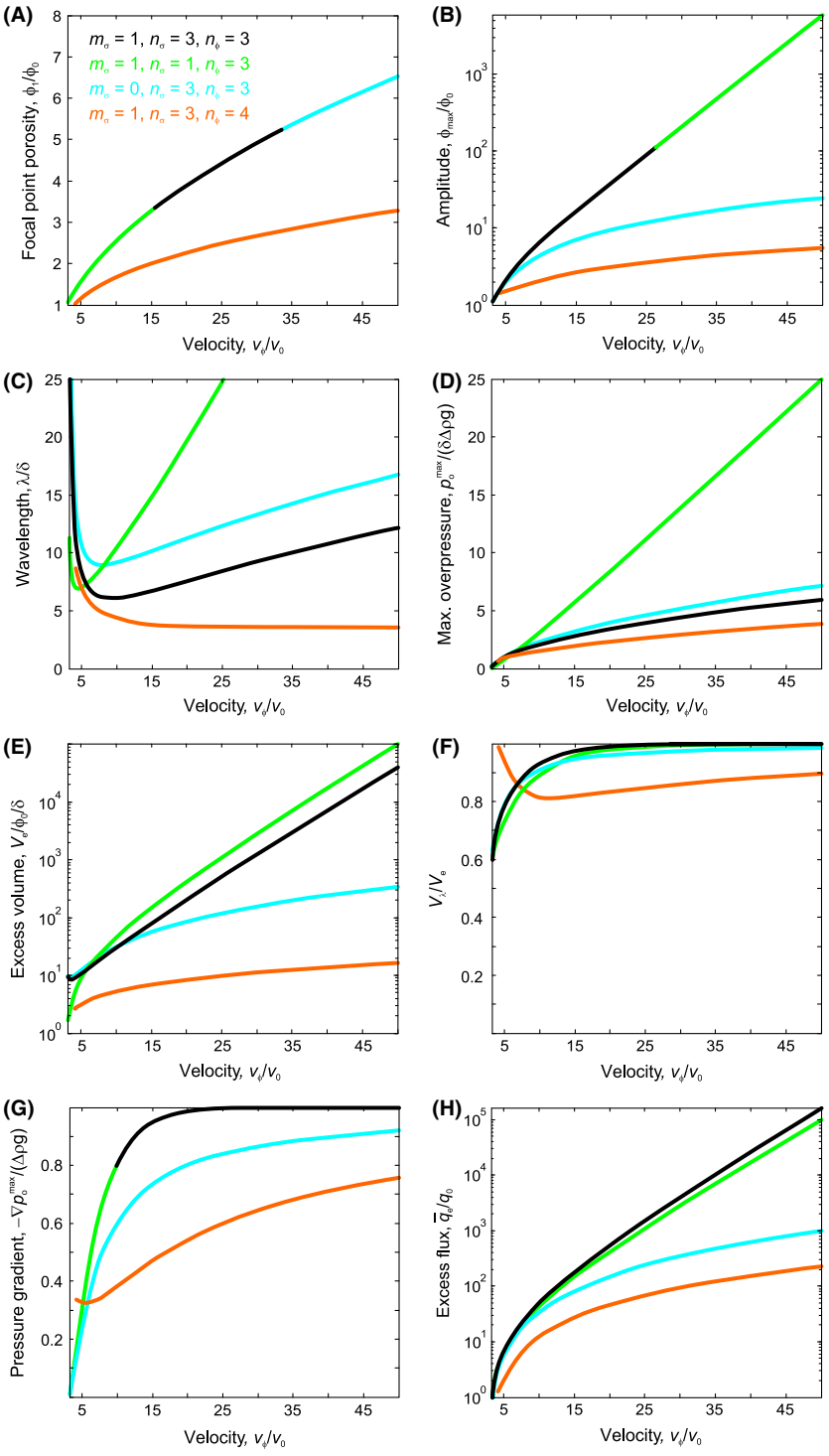

Fig. 4. Porosity wave properties in the small porosity limit ($\phi \ll \phi_d$) as a function of relative wave velocity for choices of the porosity exponents in the constitutive relations as indicated by color coding. Typical values for the exponents characterizing the porosity dependences of the permeability and effective bulk viscosity are $n_\phi = 3$ and $m_\sigma \leq 1$; a stress exponent $n_\sigma = 3$ is characteristic of dislocation creep, the viscous deformation mechanism commonly assumed for the lower crust (Ranalli 1995). The minimum relative velocity considered for each choice of exponents is $v_\phi/v_0 = n_\phi + 0.2$, slightly above the critical value, $v_\phi/v_0 = n_\phi$, for the existence of the solitary solution (Eq. 44). Continuous curves drawn in different colors indicate that the properties are identical for the corresponding exponent choices. Focal point porosity (A) and amplitude (B). Focal point porosity, ϕ_1, is dependent only on n_ϕ, and the divergence of amplitude from ϕ_1 shows that the effect of increasing the nonlinearity (i.e., m_σ) of the effective bulk viscosity is to increase amplitude. In contrast, increasing nonlinearity of the porosity–permeability relationship decreases amplitude, which is independent of n_σ. (C) Wavelength, λ, is the distance separating the overpressure extrema within a wave (Fig. 3H). (D) Maximum fluid overpressure, the maximum underpressure (i.e., effective stress) is $-p_o^{max}$, both extrema occur at ϕ_1 (Fig. 3E). (E) Excess volume (Eq. 60) correlates with amplitude except at low wave speed, whereupon it decreases with speed in solutions for high n_σ/n_ϕ. That the excess volume for the nonlinear viscous cases ($n_\sigma = 3$) becomes larger than that for the linear viscous case ($n_\sigma = 1$) at low speeds ($v_\phi/v_0 \sim 6$) indicates a shifting of the porosity toward the tails of the nonlinear viscous solution. (F) Fraction of the volume that occurs within $\pm\lambda/2$ of ϕ_{max}. (G) Maximum $-p_o$ gradient, which occurs at ϕ_{max}, unity corresponds to a hydrostatic fluid pressure gradient. (H) Average excess fluid flux associated with wave passage.

$$H = \frac{\Delta\rho g}{a_\sigma}\left(\frac{1 - v_\phi/v_0}{n_\phi(\phi/\phi_0)^{n_\phi}} + \frac{v_\phi/v_0(\phi/\phi_0)^{1-n_\phi}}{n_\phi - 1} + \ln(\phi/\phi_0)\right) \tag{56}$$

and

$$v_\phi = v_0(n_\phi - 1)\frac{A_\phi^{n_\phi}\left(\ln A_\phi^{n_\phi} + 1\right) - 1}{1 + (A_\phi - 1)n_\phi - A_\phi^{n_\phi}}, \tag{57}$$

which likewise reduces to Scott & Stevenson's (1984) result for $n_\phi = 3$. Although Eq. 57 cannot be solved ana-

lytically for amplitude, it is apparent that in the small porosity limit, amplitude is not a function of n_σ. Evaluation of the integral in Eq. 46 gives the two values of pressure at any porosity within a solitary wave (Fig. 3E) as about ϕ_{max}. Conversely, as speeds fall below that at which the overpressures at the focal point porosities of the solutions are equal, a greater proportion of the porosity shifts to the tails of the porosity distribution for the nonlinear

$$p_o = \pm\delta\Delta\rho g(n_\sigma+1)\left(\frac{1}{2^{n_\sigma}n_\phi}\frac{v_\phi}{v_0}\left[\frac{v_\phi/v_0-1}{(\phi/\phi_0)^{n_\phi}}-\ln(\phi/\phi_0)^{n_\phi}+1-\frac{v_\phi}{v_0}\frac{\left(1-\frac{n_\phi}{(\phi/\phi_0)^{n_\phi}-1}\right)}{n_\phi-1}\right]\right)^{\frac{1}{n_\sigma+1}} \tag{58}$$

The corresponding integral for depth

$$z = \pm\delta\left(\frac{n_\phi}{2}\right)^{\frac{n_\sigma}{n_\sigma+1}}\left(\frac{v_\phi}{v_0}\right)^{\frac{1}{n_\sigma+1}}\int_{\phi_{max}}^{\phi}\frac{1}{\phi}\left(\left[1-\frac{v_\phi}{v_0}\right]\left[\frac{\phi_0}{\phi}\right]^{n_\phi}+\ln\frac{\phi}{\phi_0}-1-\frac{v_\phi}{v_0}\frac{\left[1-\frac{\phi_0}{\phi}\right]^{n_\phi-1}}{n_\phi-1}\right)^{-\frac{n_\sigma}{n_\sigma+1}}d\phi \tag{59}$$

must, in general, be evaluated numerically (a Fortran computer program for this purpose is available from the author).

Because the matrix recovers to the background porosity asymptotically in a steady-state solitary wave (for $n_\sigma \geq 1$), the true wavelength is infinite (cf. Eq. 47). For practical purposes, it is desirable to define an effective wavelength, which defines the extent of the wave that includes the bulk of the anomalous porosity. To this end, the wavelength λ is taken to be interval between the points of minimum and maximum overpressure (Figs 3H and 4C). The ratio of the excess volume, that is, the total volume of fluid associated with the passage of a wave (Fig. 4E),

$$V_e = \int_{-\infty}^{\infty}(\phi-\phi_0)\,dz, \tag{60}$$

to that obtained by integrating over $\pm\lambda/2$ shows that even at low speeds, >80% of the porosity of a wave occurs within the interval $\pm\lambda/2$ about the center of wave (Fig. 4F).

The effect of nonlinear viscous rheology is best understood in terms of the overpressure at the focal point porosity ϕ_1 (Fig. 4D). The magnitude of the overpressure gradient is limited by the hydrostatic pressure gradient for the fluid phase, a limit that is approached rapidly with increasing velocity at the center of a porosity wave (black–green curve, Fig. 4G); thus, at the velocity at which the maximum pressures of the linear and nonlinear viscous solutions are equal (~5.9 v_0, black and green curves, Fig. 4D), the dilational strain rate must fall more rapidly in the nonlinear case between the ϕ_1 and ϕ_{max}, and as both ϕ_1 and ϕ_{max} are independent of n_σ, this must lead to a relatively flat-topped porosity distribution in which a greater proportion of the porosity lies within the interval $\pm\lambda/2$ case, leading to broad, poorly defined waves. This behavior is confirmed by linearization of the integral for the second moment of the solitary wave porosity distribution, which shows that in the limit $A_\phi \to 1$ or, equivalently, $v_\phi \to v_\phi^{crit}$, the moment becomes infinite if $n_\sigma \geq 3$ and explains the minima in V_e as a function of velocity for nonlinear viscous matrix rheology (black and cyan curves, Fig. 4E). The existence of the minima is of little practical consequence, because it occurs at velocities at which wavelengths are so long that the solitary waves would be indistinguishable from uniform fluid flow. Increasing n_ϕ counters this effect so that for $n_\sigma = 3$ and $n_\phi = 4$, waves are well formed at all velocities (orange curve, Fig. 4E). The instantaneous excess fluid flux, that is, the flux in excess of the background value $q_0 = v_0\phi_0$, within a wave is $q_e = v_\phi(\phi-\phi_0)$, and time-averaged fluid flux associated with wave passage (Fig. 4H) is estimated as

$$\bar{q}_e = \frac{v_\phi}{\lambda}V_e. \tag{61}$$

In the limit $v_\phi \to v_\phi^{crit}$, $\lambda \to \infty$; therefore, $\bar{q}_e/q_0$ must fall monotonically to zero with velocity, implying that there is a solitary wave solution for any value of $\bar{q}_e/q_0 > 0$.

Dynamic permeability in response to external forcing

There is no fundamental principle that dictates a balance between fluid production and transport in geological environments, but for the range of conditions investigated by numerical simulations of metamorphic compaction-driven fluid flow, this balance does develop locally (Connolly 1997, 2010). Assuming such a balance in conjunction with the solitary porosity wave solution provides a means of predicting the dynamic variations in permeability that develop from an initially steady hydrologic regime in response to metamorphic fluid production (Connolly & Podladchikov

2013). This model amounts to no more than assuming that the time-averaged permeability of a compacting system is that necessary to accommodate fluid flux associated with an external forcing (Ingebritsen & Manning 1999). The information gained by implementing the solitary wave solution in this context is insight into the instantaneous variations in porosity and pressure that develop in response to the forcing.

In a 1-d compacting system, a requirement for a balance between wave-propagated fluid transport and fluid production is that the magnitude of the time-averaged flux associated with the passage of a wave (Eq. 61) must be greater than or equal to the vertically integrated production q_s, because a wave with $|\bar{q}_e| < q_s$ would be unable to separate from its source. If $|\bar{q}_e| > q_s$, then the waves must be separated by a depth interval of $\Delta z = \lambda(|\bar{q}_e/q_s| - 1)$.

In numerical simulations, the transient dynamics of wave separation are such that $|\bar{q}_e/q_s|$ is typically <1 (Connolly 1997). This result suggests that the properties of waves expected in metamorphic environments can be predicted by equating $\bar{q}_e$ to q_s and exploiting the monotonic relationship between $\bar{q}_e$ and v_ϕ (Figs 4H and 5). In earlier work (Connolly & Podladchikov 2013), it was asserted incorrectly that solitary wave solutions do not exist for $\bar{q}_e/q_0 > 2$; in fact, solitary solutions exist for all $\bar{q}_e/q_0 > 0$, but, as remarked previously, waves that develop at small excess flux magnitudes have such long wavelengths that it is unlikely they would be distinguishable from uniform fluid flow in natural environments.

While the scenario outlined above seems the most relevant to fluid flow in ductile portions of the Earth's crust, it is conceivable that fluid production may occur so rapidly, that is, on a timescale $\ll \delta/|v_0|$, that compaction mechanisms cannot accommodate fluid production. The effect of such an imbalance may be to produce a region of increased porosity bounded by unreacted and, presumably, compacted rocks. In this scenario, the response of the system is dependent on the vertical extent, Δz, of the region of increased porosity. If the extent is small ($\Delta z \sim \delta$), then a single solitary wave will evolve from the source region in such a way as to carry the excess volume of the source region (as in Fig. 1A). The minimum in excess volume as a function of velocity for strongly nonlinear viscous rheology gives rise to potential ambiguity for such initial conditions, because the same excess volume may be accommodated in a wave with either low or high velocity. It is speculated here that the high velocity solution dominates. If the extent of the reacted porosity is large ($\Delta z \gg \delta$), then the multiple waves that evolve from the region can be expected to carry the excess flux $q_e \approx q_2 - q_0$, where q_2 is the flux through the increased porosity ϕ_2 at $p_o = 0$. Spiegelman (1993) demonstrated that waves that nucleate at the boundary between an infinite source and unreacted rocks are periodic waves in which porosity oscillates about the focal point ϕ_1 of the solitary solution (e.g., the red curve in Fig. 2E,F). However, for large porosity contrasts, that is, $\phi_2 \gg \phi_0$, the distinction is unimportant.

Example #1: 1-d viscous wave

To illustrate the application of the 1-d viscous solitary wave solution, consider an initial state characterized by $\delta \sim 100$ m, $\phi_0 \sim 10^{-4}$, $\Delta\rho g \sim 10^3$ kg m^{-3}, and $v_0 \sim -10^{-9}$ m s^{-1} ($q_0 = v_0\phi_0 = -10^{-13}$ m s^{-1}), as might be appropriate for dehydration in the lower crust at amphibolite facies conditions (i.e., temperatures of 773–923 K, Connolly & Podladchikov 2013). Taking $n_\sigma = n_\phi = 3$ and $m_\sigma = 1$ as the most probable values for the constitutive exponents, a fluid production rate of $q_s = 10^{-11}$ m s^{-1} will generate solitary waves with (black curves, Fig. 5) $\phi_{max} = 10.0$ $\phi_0 = 1.0 \times 10^{-3}$, $\lambda = 6.3$ $\delta = 630$ m, $p_o^{max} = 2.4$ $\delta\Delta\rho g = 0.24$ MPa, and a period of 1.0 $\delta/|v_0| = 1.6 \times 10^3$ years. From the period ($0.50\ \lambda/|v_0|$), or the relationship between flux and velocity (Fig. 4H), $v_\phi = -\lambda/\text{period} = 0.39$ m year^{-1} ($12.2\ v_0$) and the maximum overpressure gradient is $\nabla p_o = -0.84\ \Delta\rho g$ (Fig. 4E), that is, the fluid pressure gradient within the wave is nearly hydrostatic (cf. Eq. 5). Holding all other parameters constant, the effect of changing from power-law viscous ($n_\sigma = 3$) to linear viscous ($n_\sigma = 1$, green curves in Figs 4 and 5) matrix rheology is to double the speed, amplitude, and maximum overpressure of the waves. This effect reflects that at $v_\phi/v_0 > 5.9$ (the crossing of the green and black curves in Fig. 4E), the nonlinear wave has a greater excess volume; thus, slow waves in the nonlinear viscous case are capable of accommodating the same flux as faster waves in the linear viscous case.

Disaggregation and the compaction-driven flow regimes

Wave amplitude grows monotonically with speed in the small porosity approximation because the $1 - \phi$ and $\phi_d - \phi$ terms in Eqs 15–17 and 19 that limit the possible values of the porosity are neglected; thus, the formulation has no upper bound on porosity. Given that a granular matrix is expected to disaggregate at $\phi_d \sim 20\%$ (Arzi 1978; Auer *et al.* 1981; Ashby 1988; Vigneresse *et al.* 1996), the $\phi_d - \phi$ term is likely to dominate wave behavior before the dampening effects of the $1 - \phi$ terms become significant. Elsewhere, it has been shown that for constitutive relations that do not account for disaggregation, the $1 - \phi$ terms are unimportant at absolute porosities of ~25% for typical choices of the exponents n_σ, n_ϕ, b_ϕ, and m_σ (Connolly & Podladchikov 2000; a Fortran computer program that solves the large porosity formulation is available upon request). Accordingly, the effect of disaggregation is assessed here by an intermediate porosity approximation in which the $\phi_d - \phi$ term of Eq. 19 is

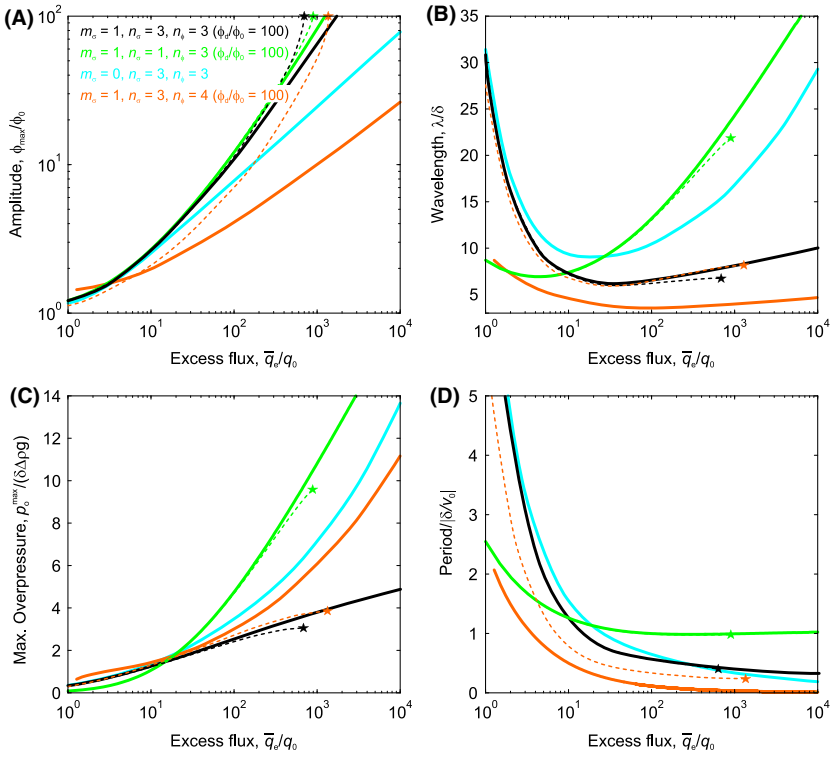

Fig. 5. Porosity wave properties as a function of the average excess fluid flux associated with wave passage for the exponent choices indicated by the legend and color coding. Solid curves are for the small porosity limit ($\phi \ll \phi_d$) as in Fig. 4; dashed curves show the influence of a disaggregation in the intermediate porosity limit ($\phi_d \ll 1 - \phi$) for the specific case that $\phi_d/\phi_0 = 100$, discussed later in the text (Fig. 6). Star symbol at the end of dashed curves indicates the disaggregation condition. Properties of waves likely to be generated in natural settings in response to fluid production can be estimated by equating vertically integrated fluid production to the average excess flux.

retained, but porosity terms of order 1 (i.e., $1 - \phi$ and $1 - \phi^{1/n_\sigma}$) are dropped to obtain

$$H = \frac{\Delta\rho g}{\phi_0^{m_\sigma} c_\sigma} \int \left[\left(\frac{\phi_0}{\phi}\right)^{m_\sigma} - \left(\frac{\phi_0}{\phi}\right)^{n_\phi + m_\sigma} + \frac{v_\phi}{v_0} \left(\left[\frac{\phi_0}{\phi}\right]^{n_\phi + m_\sigma} - \left[\frac{\phi_0}{\phi}\right]^{n_\phi + m_\sigma - 1} \right) \right] \Big/ \left[\frac{\phi_d}{|\phi_d - \phi|} \right]^{n_\sigma - 1/2} d\phi \qquad (62)$$

for the properties of waves with porosities approaching ϕ_d. As the denominator of the integrand in Eq. 62 becomes infinite at $\phi = \phi_d$, H must have a maximum at ϕ_d, and if $H(\phi_d) < H(\phi_0)$ (Fig. 3C), then there is no closed contour of the function U that connects the background porosity to an increased level of porosity (Eq. 41, Fig. 3F) and no solitary solution is possible. Because the integrand of Eq. 62 is simply the combined integrands of Eq. 54, scaled by the disaggregation term, the effects of varying the exponents n_ϕ, n_σ, and m_σ are readily separated. Specifically, lowering n_σ or raising n_ϕ or m_σ increases $H(\phi_d)$ relative to $H(\phi_0)$, extending the range of solitary wave velocities that the matrix can sustain without disaggregating (Fig. 6A). In contrast to the small porosity limit where H, and therefore wave amplitude, is independent of the stress exponent n_σ, in the intermediate porosity limit, although the focal point porosity ϕ_1, and therefore p_o^{max} (Fig. 6C), remains independent of n_σ, the relation between amplitude and velocity is dependent on n_σ. For $n_\sigma = n_\phi = 3$, this dependence is prominent for $\phi/\phi_d > 0.1$ (black curves, Fig. 6A) and is even more pronounced with increasing nonlinearity in the porosity–permeability relationship (orange curves, Fig. 6A). Because the effect of the disaggregation term is to weaken the matrix with increasing porosity, its effect is to sharpen the porosity distribution within solitary waves, akin to the result of increasing m_σ, leading to an increase in excess volume compared to models that do not account for disaggregation.

By solving for the solitary wave velocity at which $H(\phi_d) = H(\phi_0)$ and computing the corresponding value of $\bar{q}_c$ (Eq. 61), it is possible to estimate the range of fluid production rates that can be sustained without causing the solid matrix to become fluidized. For example, taking $n_\phi = 3$ and $\phi_d/\phi_0 = 100$, fluid production rates of 700–900 $|q_0|$ are adequate to induce fluidization (Fig. 7); for comparison, to cause fluidization by, albeit unstable, uniform flow, the required fluid production rates are $|q_0|(\phi_d/\phi_0)^{n_\phi}$, that is, 10^6 $|q_0|$. Thus, porosity waves have the potential to strongly enhance weak flow perturbations. In terms of fluxes, the lower limit of the solitary wave regime corresponds to $\bar{q}_c = 0$; thus, the periodic regime can only be induced by a negative vertically integrated fluid production rate such as would result from the consumption of fluids by retrograde hydration reactions. Alterna-

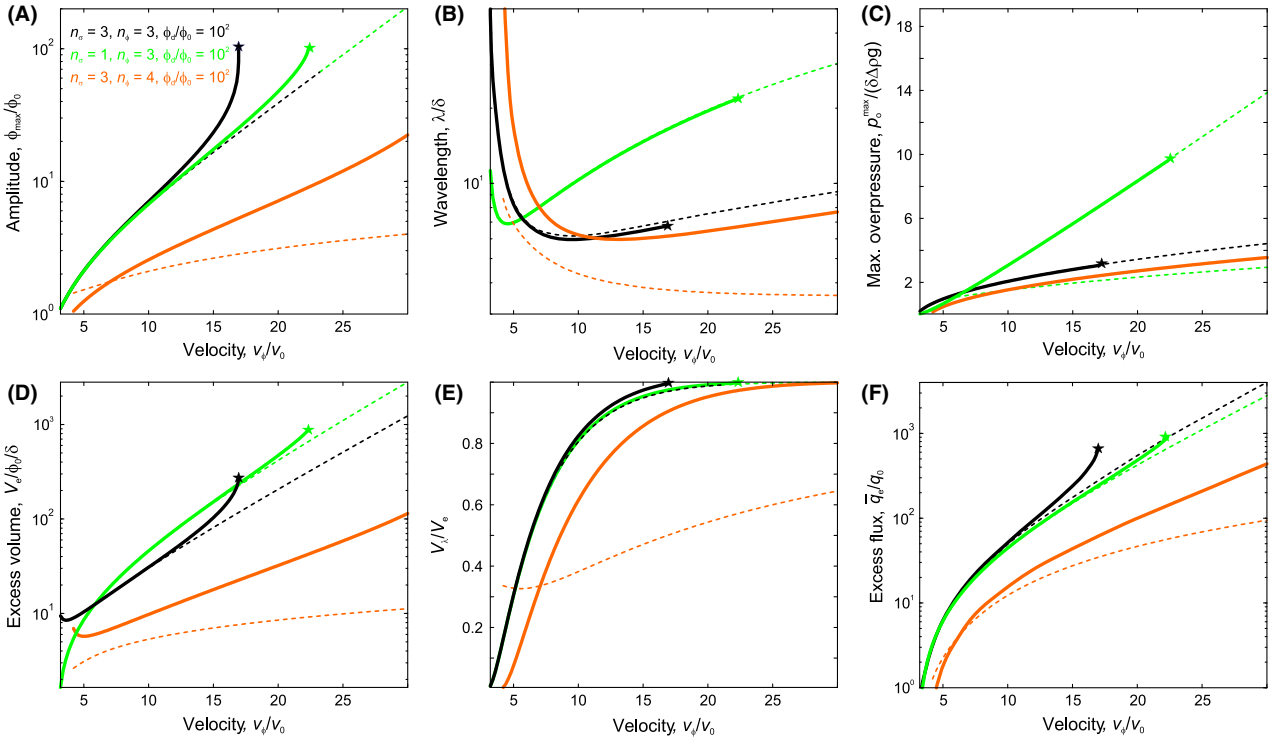

Fig. 6. Porosity wave properties in the intermediate porosity limit ($\phi_d \ll 1 - \phi$) as a function of velocity for a disaggregation porosity ϕ_d a hundred times greater than ϕ_0. All examples are for $m_\sigma = 1$ with other exponents of the formulation as indicated by the legend and color coding. The star symbol indicates the disaggregation condition. Dashed curves show the corresponding properties for the small porosity limit as in Fig. 4. The solutions show that the effect of disaggregation is strongly dependent on both n_ϕ and n_σ; for $n_\phi = 3$ the disaggregation effect becomes significant if ϕ_{max} is within an order of magnitude of ϕ_d and is amplified by increasing n_σ. Properties for these solutions are shown as a function of $\bar{q}_e$ in Fig. 5.

tively, for waves induced by a perturbation defined in terms of an excess volume (e.g., Fig. 1), the periodic solution requires negative excess volume, that is, an obstruction (Spiegelman 1993) to a region of uniform flow. The appearance of periodic waves in numerical simulations (e.g., Fig. 1A or Connolly 1997) reflects the dynamics of solitary wave separation, in which over-compaction of the matrix obstructs the background flow.

DISCUSSION

This study has explored the behavior of the solitary porosity wave solution to the compaction equations in 1-d viscous media. The solution provides a simple means of estimating the scales of pressure and porosity (or permeability) variations as a function of fluid production rates and constitutive relations. Although porosity waves have been posited as a mechanism for fluid flow in the lower crust (Suetnova *et al.* 1994; Connolly 1997; Gliko *et al.* 1999; Ague 2014; Tian & Ague 2014), their expression in nature would be complicated by a number of factors. These factors, which include geometry, lithological heterogeneity, tectonic stress, and rheological variations, have been reviewed elsewhere (Connolly & Podladchikov 2004, 2013). Here, some aspects of this earlier review, which are particularly relevant to potential applications of the 1-d solitary wave solution, are recapitulated in the context of a conceptual model for compaction-driven fluid flow in the lower crust (Fig. 8).

Linear or nonlinear viscous rheology?

Even if the viscous deformation mechanism is nonlinear, in rocks undergoing simultaneous compaction and shear deformation, it does not necessarily follow that effective viscous rheology for the compaction process is nonlinear. Both compaction and macroscopic shear deformation are accomplished by microscopic shear. Thus, if a rock is simultaneously subject to both modes of deformation, then they must be accommodated by the same microscopic mechanism. This mechanism is determined by the largest of the stresses responsible for deformation, $|\Delta\sigma|$ or $|p_o|$, with the result that if the stresses are of different magnitude, the viscous response to the inferior stress is approximately linear and determined by effective viscosity resulting from the deformation induced by the superior stress. Regardless of magnitude, far-field tectonic stress facilitates compaction

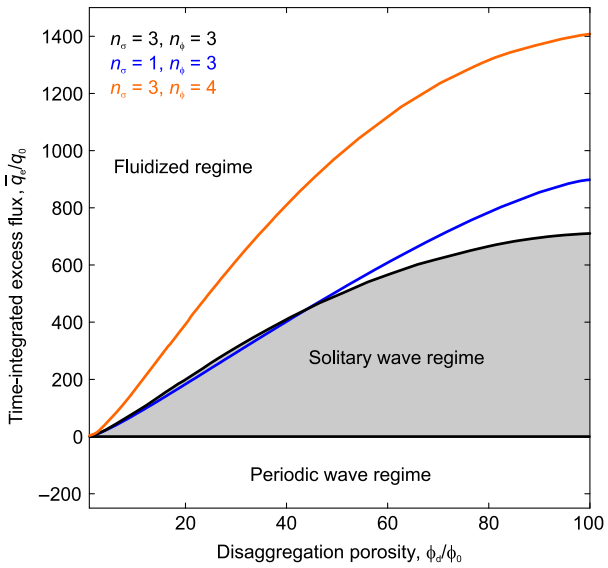

Fig. 7. Phase diagram depicting the hydrologic regimes predicted by the intermediate porosity limit solitary wave solution as a function of the disaggregation porosity and excess flux. The regime that develops in response to fluid production can be predicted by equating the magnitude of the excess flux carried by the waves to the vertically integrated fluid production $\bar{q}_s$. The boundary between the solitary wave and fluidized regime is dependent on the exponents m_σ, n_σ, and n_ϕ; it is shown for $m_\phi = 1$, with other exponents as indicated by the inset and color coding. Solitary waves become progressively more diffuse and indistinguishable from uniform flow as $\bar{q}_e/q_0 \rightarrow 0$. Periodic wave trains develop in response to negative fluid production, for example, the consumption of fluids by hydration reactions, or an obstruction to the background porosity (Spiegelman 1993). In nature, such periodic wave trains would decay to uniform flow.

by lowering the effective viscosity of the solid matrix (Tumarkina *et al.* 2011).

3-d Geometry and non-viscous rheology

As remarked earlier, the 1-d solitary wave solution is unstable with respect to spherical solitary waves in three dimensions (Wiggins & Spiegelman 1995). However, as wave speeds increase, the overpressure gradient in solitary waves rapidly approaches the limit (i.e., $-[1-\phi]\Delta\rho g$) imposed by the fluid hydrostat (Fig. 4G). At this condition, the velocity and porosity distribution along the vertical axis of the 1- and 3-d waves are essentially identical, and the excess volume of the 3-d wave can be estimated by applying spherical symmetry to porosity distribution of the 1-d wave (Connolly & Podladchikov 2007). Transient models of multidimensional waves suggest that they collect fluid from a source region of area $\sim\pi\lambda^2$ (Wiggins & Spiegelman 1995). Thus, the properties of the 3-d waves that would initiate in response to fluid production can be predicted by equating the product of vertically integrated fluid production rate and the source area, $Q_s = \pi\lambda^2 q_s$, with the volumetric transport rate

$$Q = \frac{v_\phi}{\lambda}\int_0^\infty 4\pi r^2(\phi-\phi_0)\mathrm{d}r, \tag{63}$$

where the integral is the 3-d excess fluid volume associated with the wave and is approximated by using the 1-d solitary wave solution for the radial porosity distribution. In practice, because λ varies as a function of q_s, solving $Q_s = Q$ is an iterative problem.

Example #2: 3-d viscous wave

To illustrate the consequences of 3-d geometry, consider the same parameters as in Example #1. Taking the 1-d wavelength, $\lambda = 6.3\ \delta$, as an initial estimate for the 3-d solution, the required fluid transport rate is $Q/|q_0\delta^2| = q_s\pi\lambda^2/|q_0\delta^2| = 100\ \pi\ 6.3^2 = 1.25 \times 10^4$. For this value of Q, $v_\phi/v_0 = 29$ (black curve, Fig. 10) and $\lambda/\delta = 9.1$ (black curve, Fig. 4C). Using this revised estimate of wavelength, $Q/|q_0\delta^2| = 2.6 \times 10^4$, which in turn yields new velocity and wavelength estimates of $v_\phi/v_0 = 37.6$ and $\lambda/\delta = 11.0$. After three iterations, successive refinement of the estimates for fluid transport rate, velocity, and wavelength by this method yields: $Q = 37.9 \times 10^{-5}$ m^3 s^{-1}, $\lambda = 11.0\ \ \delta = 1100$ m, $\ v_\phi = 41.4\ \ v_0 = -1.31$ m year^{-1}, $p_o^{max} = 5.35\ \ \delta\Delta\rho g = 5.35$ MPa, and $\phi_{max} = 1390\ \ \phi_0 = 0.139$ for the 3-d wave. This result demonstrates that increased spatial focusing of fluid flow caused by 3-d effects has the capacity to generate both the large porosities necessary to cause disaggregation and/or the overpressures necessary to induce brittle (plastic) failure.

Thermal activation

Thermal activation will, generally, lead to an upward increase in the effective shear viscosity of the lower crust on a length scale l_A that is dependent on the activation energy of the viscous mechanism and the geothermal gradient, but typically ~1 km (Connolly & Podladchikov 2013). Consequently, all other factors being equal, the compaction length scale δ will increase upward through the crust as $\sqrt[n_\sigma+1]{\exp(z/l_A)}$, that is, by a factor of ~10 over a vertical interval distance of 6–8 l_A. This variation has consequences for the relevance of the steady-state solution, which assumes a constant effective shear viscosity. Provided $\delta < l_A$, the variation in shear viscosity due to thermal activation is weak on the porosity wave length-scale. In this case, quasi-steady state waves that closely approximate the steady-state solution can be expected to develop. The evolution of such quasi-steady state waves can be anticipated from the steady-state solution given that the waves are likely to conserve excess volume (Fig. 4E, Connolly & Podladchikov 2013). As δ becomes comparable to l_A, multidimensional waves flatten to sill-like structures. Although these structures superficially resemble the 1-d steady-state solitary wave solution, their vertical dimension is dictated

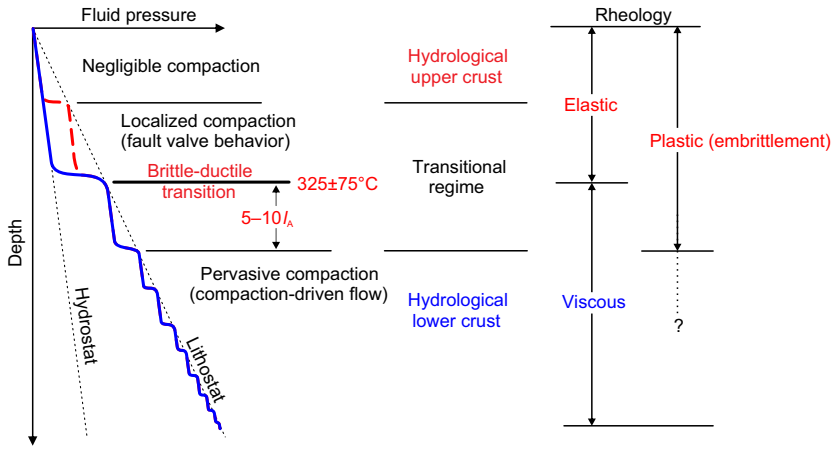

Fig. 8. Conceptual model of the hydrologic regimes that would result from superimposing thermally activated compaction on crustal column with heterogeneous permeability (Connolly & Podladchikov 2013). In the upper crustal regime, faulting maintains such high permeabilities that negligible deviation from hydrostatic fluid pressure is adequate to drive fluid circulation (Zoback & Townend 2001). This regime is limited at depth by the conditions at which localized compaction becomes an effective mechanism for sealing fault-generated permeability (Gratier *et al.* 2003; Tenthorey & Cox 2006). At greater depth, pervasive compaction and/or metamorphic fluid production may generate transient fluid overpressure that is periodically relieved by faulting (Sibson 1992). At the brittle–ductile transition (i.e., the base of the seismogenic zone), it is improbable that pervasive compaction can keep pace with metamorphic fluid production; thus, the transitional hydrologic regime is likely to persist over an interval that extends ~10 l_A below the brittle–ductile transition, where l_A is the characteristic length scale for variation in the ductile rheology (typically ~1 km, Connolly & Podladchikov 2013). Beneath the transitional regime, pervasive compaction is capable of generating hydraulic seals and fluid, if present, is at near lithostatic pressure. Within this lowermost regime, fluid flow is truly compaction-driven. In the absence of fluid production, the tendency of both time and depth is to decrease the wavelength of the fluid pressure compartments, resulting in a near-steady state. Barring the possibility of a subcrustal fluid source, the flux in this near-steady regime must decrease with depth. Thus, the magnitude of the perturbation caused by fluid production to the lower crustal regime is dependent on its depth. In the deepest portion of the crust, the rheology is viscous as assumed in the formulation presented here. Upward strengthening of the viscous rheology would cause porosity waves to provoke elastic and plastic deformation mechanisms at shallower levels. Because viscous porosity waves are associated with negative effective pressure anomalies, $\sim\lambda\Delta\rho g/2$, the first deviation from viscous behavior is likely to be viscoplastic. Viscoplastic rheology causes fluid flow to be focused into tubelike channels (Connolly & Podladchikov 2007; Connolly 2010). At still shallower depths, viscous compaction becomes entirely ineffective, leading to a viscoelastic transition. In numerical models, such a viscoelastic transition causes lower crustal solitary porosity waves to dissipate as porosity-pressure surges in the upper crust (Connolly & Podladchikov 1998).

by l_A and they slow exponentially as they propagate upward (Connolly 1997; Connolly & Podladchikov 1998). This behavior suggests that if porosity waves develop on a geologically relevant length scale at depth within the crust, then, in the absence of other deformation mechanisms, they will tend to stagnate below the brittle–ductile transition (Fig. 8).

Example #3: thermal activation

Consider a 1-d solitary porosity wave with initial properties $\delta_i \sim 100$ m, $\lambda = 630$ m, $p_o^{max} = 0.24$ MPa, and $v_\phi = 12.2\ v_0$, as in Example #1, which propagates upward through a cooling, but otherwise uniform crust, characterized by $l_A \sim 1$ km. The initial dimensionless excess volume $(V_c/\delta_i/\phi_0)$ of the wave is 41.4 (black curve, Fig. 4H). After the wave rises 5 km, the local compaction length increases to $\delta = \delta_i \sqrt[n_\sigma+1]{\exp(\Delta z/l_A)} = 350$ m. If the wave conserves its dimensional excess volume (V_c), then the dimensionless excess volume $V_c/\delta/\phi_0$ must decrease to 11.9. For this new dimensionless excess volume, the wave velocity is $v_\phi/v_0 = 5.6$ (Fig. 4H), and its wavelength and maximum overpressure increase to 2200 m (Fig. 4C) and 0.40 MPa (Fig. 4D), respectively. As this wavelength is greater than l_A, the steady-state solution most likely overestimates both velocity and wavelength (Connolly & Podladchikov 1998).

Viscoplastic rheology

In the viscous limit, a solitary wave is associated with a maximum fluid overpressure of $\sim\lambda\Delta\rho g/2$ that grows as the wave propagates upward into cooler rocks. As rocks have little tensile strength (Gueguen *et al.* 2004), it is probable that such fluid overpressures would induce hydrofracture and/or other plastic dilational mechanisms. Brittle deformation associated with active metamorphism (Etheridge *et al.* 1984; Simpson 1998) is broadly consistent with the notions that embrittlement occurs at high fluid pressure and on spatial scales $\ll\delta$. In this scenario, the effect of plastic weakening can be simulated by reducing the coefficient of viscous flow by a factor of $R^{n_\sigma+1}$ for $p_o > 0$. The ad hoc factor R can be adjusted to match the presumed yield stress, σ_y, of the plastic mechanism. In 1-d numerical models that use this approximation, asymmetrical, steady-state solitary waves develop in which a small overpressured region is fed by a much larger underpressured region (Fig. 1D–F). In the small porosity limit, such solutions are

permitted because the hydraulic potential H (Eq. 54), which determines the shape of the viscous solitary wave, is independent of A and n_σ. Thus, both the upper and lower portions of the viscoplastic solitary wave are given by the viscous solitary wave solution with the sole modification that the compaction length scale in the overpressured region is

$$\delta_p = \delta R. \tag{64}$$

As the effect of weakening is to reduce the timescale during decompaction to $\tau_p = \delta R/|v_0|$, it is unsurprising that in three dimensions the overpressured region develops the spherical porosity distribution of the viscous solution on the length scale δ_p, which then recovers in the underpressured region to ϕ_0 on the length scale δ, giving rise to a wave shape similar to that of a cigar aligned in the direction of flow with the lit end upward (Connolly & Podladchikov 2007). In contrast to the 1-d case, the asymmetry of the pressure distribution for such a wave obviates a true steady state. Specifically, numerical simulations (Fig. 9) show that the underpressured lower portion of the wave drains more fluid from surrounding matrix than is expelled into the matrix by the overpressured upper portion with the result that viscoplastic solitary waves grow with time. The imbalance in fluxes has the consequence that waves leave a tubelike channel, with porosities slightly $>\phi_0$, in their wake. This channel localizes subsequent fluid flow because it is surrounded by an interval of compacted matrix, with $\phi < \phi_0$, of radius δ.

Although the 3-d viscoplastic solitary wave solution is not steady state, at any point in time its properties are well represented by a geometric transformation of the viscous steady-state solution. Neglecting the small fraction of the excess volume associated with the overpressured portion of the wave, the porosity distribution of the viscoplastic wave approximates the lower half of a prolate ellipsoid with semi-major axis $\lambda_p = \lambda/2$ and semi-minor axis of $R\lambda/2$, where λ is the wavelength of a viscous wave with the same velocity as the viscoplastic wave (Fig. 4C). As the velocity–amplitude relation (Fig. 4B) is, for $v_\phi/v_0 > \sim 2n_\phi$, essentially independent of the dimension of the solution, the fluid transport rate for the viscoplastic case is

$$Q_p = \frac{Q}{2} R^2, \tag{65}$$

where Q is the transport rate for the spherical viscous solitary wave (Eq. 63). In contrast to the 3-d viscous case,

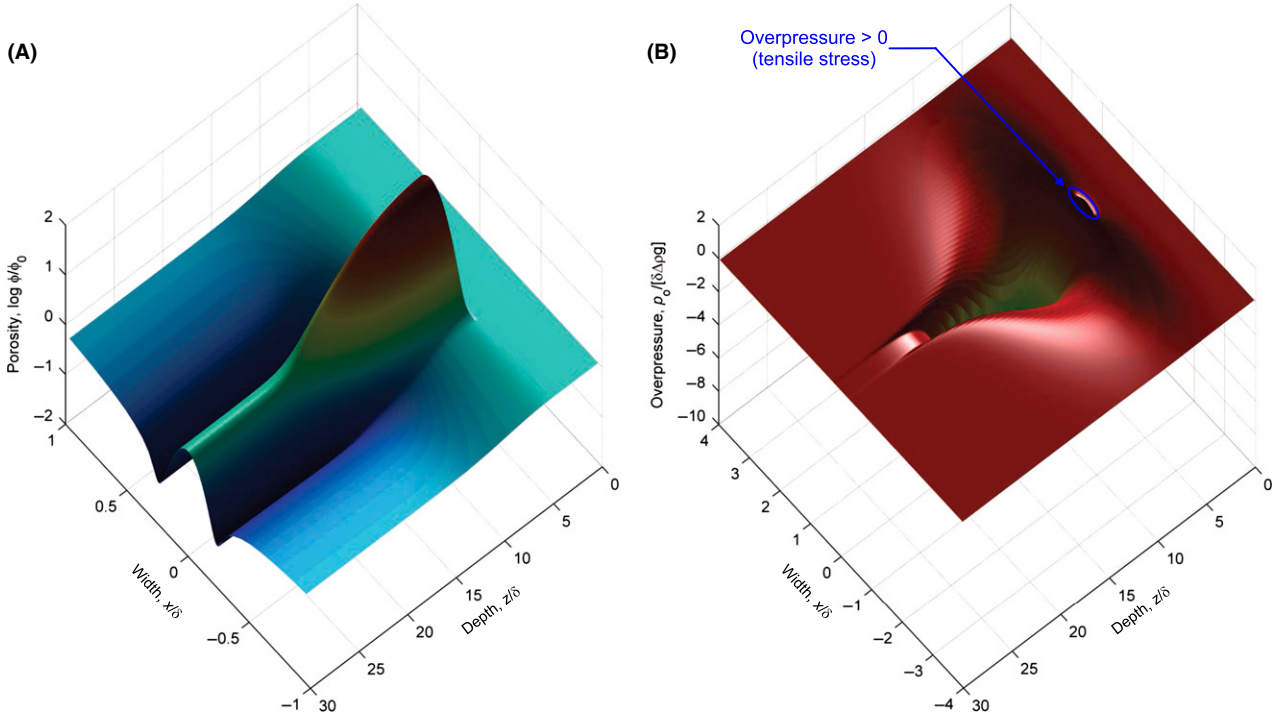

Fig. 9. Two-dimensional numerical simulation of a solitary porosity wave in a viscoplastic matrix. (A) Porosity; (B) fluid overpressure. The axial porosity and overpressure profiles of the wave are identical to the 1-d case (Fig. 1C,D), but in the 2-d case, the asymmetric overpressure distribution causes compaction of the background porosity on either side of the wave, leaving a tubelike channel that localizes subsequent fluid flow; the logarithmic scale for porosity emphasizes this effect. Numerical simulations (B. J. P. Kaus, pers. comm. 2005) have confirmed that 3-d solitary waves in a viscoplastic matrix have radial symmetry orthogonal to the direction of propagation as in the viscous limit (Wiggins & Spiegelman 1995); thus, the 2-d wave shown here corresponds to the axial section of a 3-d wave.

where fluid is collected from an area proportional to λ, in the viscoplastic case, the horizontal radius of the wave is small in comparison with δ (Connolly & Podladchikov 2007; Connolly 2010). Thus, 3-d viscoplastic waves collect fluid from a source area of $\sim\pi(\delta/2)^2$ regardless of the vertically integrated fluid production rate q_s. Consequently, for a given q_s, the initial velocity of a viscoplastic wave can be estimated by equating the fluid production likely to be collected by the wave, $q_s\pi(\delta/2)^2$, with Q_p. Making use of Eq. 65, the fluid transport rate of the viscous solution with the same velocity–amplitude relation as the viscoplastic wave is then

$$Q = \frac{\pi}{2} q_s \left(\frac{\delta}{R}\right)^2. \tag{66}$$

From this value of Q, the relation between Q and v_ϕ for the 3-d viscous solution (Fig. 10) yields the velocity of the viscoplastic wave. The remaining properties of the wave are then recovered from the 1-d viscous solution as a function of this velocity with the modifications: $\lambda_p = \lambda/2$, $p_o^{\min} = -p_o^{\max}$, and the maximum overpressure, ostensibly σ_y, is $-Rp_o^{\min}$.

It is possible to derive rigorous expressions for the effective viscosity resulting from various types of plastic yielding and the corresponding 1-d solitary wave solutions (Yarushina 2009), but the viscoplastic solution for brittle yielding is well represented by the simple model presented here (Eq. 65) if the parameter R is adjusted to match σ_y. In particular, that viscoplastic matrix rheology causes solitary waves to grow with time and channelize fluid flow are likely to be robust predictions. Unfortunately, the nonsteady character of the 3-d solution simulated by the simple model creates an unrealistic situation in which the implied brittle yield strength grows with time. Although a multidimensional transient model with true brittle yielding remains to be investigated, in such a model $p_o^{\max}$ is constrained by σ_y, while the volume of the overpressured portion at σ_y can be expected to increase with time. Such effects could substantially alter the results of the geometric model (i.e., Eq. 65) used to estimate the fluid transport rate here.

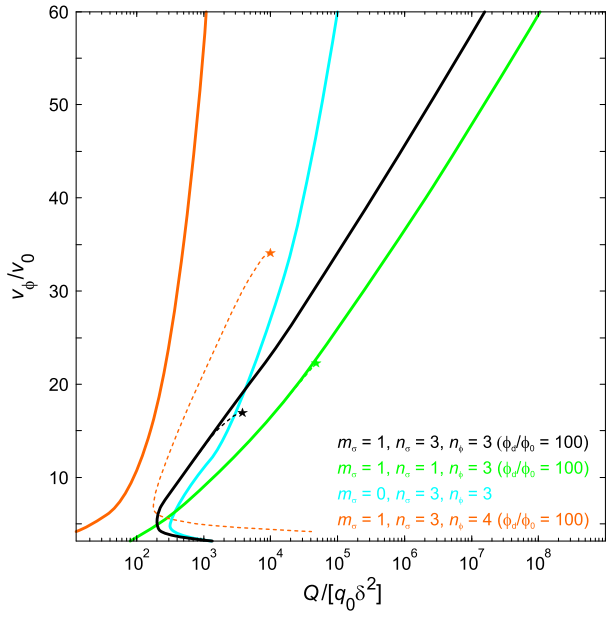

Fig. 10. Wave velocity as a function of volumetric fluid transport rate (Q) by spherically symmetrical 3-d porosity waves (Wiggins & Spiegelman 1995) for exponent choices as indicated by the legend. For velocities at which the fluid pressure gradient (Fig. 4g) is nearly hydrostatic, the properties of the 1- and 3-d solution are essentially identical; thus, at these conditions, the velocity can be used to predict 3-d wave properties from the 1-d solution (Fig. 4, and Examples #2 and #3). Where velocity is not a monotonic function of Q, it is probable that the high velocity (short wavelength) solution dominates.

Example #4: 3-d viscoplastic wave

To quantitatively illustrate the consequences of the foregoing model for viscoplastic waves, consider parameters as in Example #1, but with $R = 0.1$. The fluid transport rate of the corresponding 3-d viscous wave (Eq. 66) is $Q/|q_0\delta^2| = (q_s/|q_0|)\,\pi/(2R^2) = 1.57 \times 10^4$. From the relationship between Q and v_ϕ (Fig. 10), $v_\phi = 25.3\ v_0 = -0.79$ m year^{-1}, and for this velocity (Fig. 4), $\phi_{\max} = 94.5\ \ \phi_0 = 9.45 \times 10^{-3}$, $\lambda_p = \lambda/2 = 4.24\ \ \delta = 424$ m, and $p_o^{\min} = -p_o^{\max} = -3.99\ \delta\Delta\rho g = -3.99$ MPa. From the model geometry, the actual fluid transport rate (Eq. 65) $Q_p = 1.57 \times 10^4\ (R^2/2)\ |q_0\delta^2| = 2.48$ m^3 year^{-1}; the maximum fluid overpressure $\sigma_y = -Rp_o^{\min} = 0.399$ MPa; the radius of the wave and the channel left in its wake is $\lambda_p = \lambda/2 = 4.24\ \delta = 424$ m; and the channels would have a spacing $\sim\delta = 100$ m.

Viscoelastic rheology

The omnipresent elastic response of the rock matrix (or pore fluid) becomes significant as the effective bulk viscosity of the matrix increases. Such an increase is to be expected as the crust strengthens upward toward the brittle–ductile transition and also locally in response to decreases in porosity. In general, steady-state solutions for Maxwell viscoelastic porous media take the form of heteroclinic shock waves that connect two distinct levels (ϕ_0 and ϕ_1 in the present formulation) of porosity (Rice 1992; Connolly & Podladchikov 1998). These can be understood in terms of the oscillating ball analogy to viscous solution (Fig. 2) in that elasticity acts similarly to friction on the motion of the ball, which dampens the oscillations of the ball so that it comes to rest at the focal point. Fluid compressibility and poroelasticity have opposite effects (Connolly & Podladchikov 1998): in a system composed of a viscous, inelastic, matrix and a compressible fluid the focal point porosity ϕ_1 is at the leading edge of the shock and the background porosity ϕ_0 is in its wake; whereas in a system composed of a viscoelastic

matrix and a incompressible fluid the background porosity ϕ_0 is at the leading edge of the shock and the focal point porosity ϕ_1 is in its wake. Thus, the relative magnitude of the fluid and matrix elastic compressibilities controls whether the elevated porosity ϕ_1 is at the leading edge or in the wake of the viscoelastic. Most applications of elastic and viscoelastic porosity wave solutions in the geological literature (Rice 1992; Revil & Cathles 2002; Miller *et al.* 2002; Chaveau & Kaminski 2008; Joshi *et al.* 2012) assume negligible fluid compressibility. The heteroclinic character of viscoelastic solutions has the peculiar implication that the non-dissipative elastic rheology leads to dissipative porosity shock waves. In transient models, a viscoelastic transition caused by upward strengthening provokes a rapid transition from lower crustal solitary waves, which are well approximated by the viscous limit, to porosity fluid pressure surges in the upper crust (Connolly & Podladchikov 1998). Even if both solid and fluid constituents are considered to be incompressible, surface tension as incorporated in the formulation of Bercovici *et al.* (2001) has the effect of generating a Kelvin viscoelastic compaction rheology. The Kelvin limit may be of relevance at the small porosities thought to be characteristic of the lower crust (Connolly & Podladchikov 2013; Ague 2014) at which surface tension may inhibit compaction.

CONCLUDING REMARKS

There is no smoking gun as evidence for the existence of porosity waves as a mechanism for fluid flow in the lower crust. The porosity wave model is the mathematical consequence of a set of physical assumptions that are generally thought to apply to lower crustal processes. Most prominent among these assumptions are that lower crustal rocks compact by viscous creep and that fluid flow is described by Darcy's law. The virtue of the porosity wave model is that it represents a physically consistent steady state and provides a simple means of anticipating the hydrodynamic response of the lower crust to perturbations such as fluid production. The formulation developed here has small ($\phi \ll \phi_d$) and intermediate ($\phi_d \gg 1 - \phi$) porosity approximations that are dependent only on relative porosity (ϕ/ϕ_0); material properties or, alternatively, scales (ϕ_0, $|v_0|$, and δ); two exponents (m_σ and n_ϕ) that characterize the porosity dependence of the effective bulk viscosity and permeability of the rock matrix; and an exponent (n_σ) that characterizes the stress dependence of effect shear viscosity of the rock matrix. In particular, the role of the stress exponent n_σ has not been considered in previous studies. The most surprising feature resulting from this nonlinearity is that it appears to admit a finite-wavelength solitary solution for shear-thickening ($n_\sigma < 1$) viscous mechanisms. Finite-wavelength solitary porosity waves are of interest because they permit deformation-propagated fluid flow through an initially impermeable matrix (Connolly & Podladchikov 1998). For the shear-thinning ($n_\sigma > 1$) viscous mechanisms thought to be characteristic of the lower crust (Kohlstedt *et al.* 1995; Ranalli 1995), the stress exponent does not fundamentally change the behavior described for the linear viscous case (Fowler 1984; Richter & McKenzie 1984; Scott & Stevenson 1984). However, somewhat counterintuitively, at low velocities ($v_\phi/v_0 < \sim 6$) nonlinearity results in poorly defined waves in which a greater proportion of the porosity lies in the tails of the waves compared to the porosity distribution of the linear viscous case. At higher velocities, this trend reverses so that a greater proportion of the fluid occurs near the center of mass of a wave in the nonlinear case. Disaggregation effects and increasing the nonlinearity of the effective bulk viscosity also lead to more sharply defined porosity distributions.

The ansatz that porosity waves evolve to accommodate the vertically integrated fluid production rate q_s in natural systems has the trivial consequence that in the 1-d limit the effective permeability resulting from the porosity wave mechanism, $k_{\text{effective}} \approx k_0 \bar{q}_e/q_0$, is $\sim k_0 q_s/|q_0|$, where k_0 and q_0 are the background permeability and fluid flux, respectively, and $\bar{q}_e$ is time-averaged flux carried by a wave (Fig. 4H). Local variations in permeability are significantly larger, for example, in the 1-d quantitative example considered here (Example #1), the maximum local permeability $k_0[\phi_{\max}/\phi_0]^{n_\phi}$ is an order of magnitude greater than the effective permeability and three orders of magnitude greater than k_0. Spatial effects associated with 3-d porosity waves lead to substantially higher effective permeability. In the quantitative example of the 3-d viscous case (Example #2), $k_{\text{effective}} \approx k_0 Q/\left|q_0\pi(\lambda/2)^2\right| = 3990\ k_0$, and for the viscoplastic case (Example #4), $k_{\text{effective}} \approx k_0 Q_p/|q_0\pi\left(R\lambda_p\right)^2| = 139\ k_0$. These results are dependent on highly uncertain, but plausible, values for q_s and the scales ϕ_0, $|v_0|$, and δ (Connolly & Podladchikov 2013). In general, q_s can be estimated from knowledge of the lithology of interest and the geodynamic scenario responsible for fluid production. The background porosity ϕ_0 and fluid velocity v_0 are roughly constrained from relatively well-known physical properties and theoretical considerations, leaving the compaction length scale δ as the greatest source of uncertainty in that it combines the hydraulic and rheological properties of the combined fluid-rock system. At present, it seems that the spatial scales of compaction-driven flow phenomena offer the most accurate means of estimating the compaction length in natural environments.

ACKNOWLEDGEMENTS

This paper was improved by reviews from Jay Ague and Martin Appold and by the editorial direction of Tom

Gleeson, Steve Ingebritsen, and Craig Manning. The original version of this paper was written while the author was a guest of the Centre of Advanced Studies at the Norwegian Academy of Science and Letters for the 'Dynamics of Fluid Rock Systems' project led by Bjorn Jamtveit between 2000 and 2001.

REFERENCES

Ague JJ (2014) Fluid flow in the deep crust. In: *Treatise on Geochemistry* (eds Holland HD, Turekian KK), 2nd edn, pp. 203–47. Elsevier, Oxford.

Appold MS, Nunn JA (2002) Numerical models of petroleum migration via buoyancy-driven porosity waves in viscously deformable sediments. *Geofluids*, **2**, 233–47.

Arzi AA (1978) Critical phenomena in rheology of partially melted rocks. *Tectonophysics*, **44**, 173–84.

Ashby MF (1988) The modeling of hot isostatic pressing. In: *Proceedings HIP: Hot Isostatic Pressing – Theories and Applications* (ed. Garvare T), pp. 29–40. Centek, Lulea, Sweden.

Audet DM, Fowler AC (1992) A mathematical model for compaction in sedimentary basins. *Geophysical Journal International*, **110**, 577–90.

Auer F, Berckhemer H, Oehlschlegel G (1981) Steady-state creep of fine-grain granite at partial melting. *Journal of Geophysics-Zeitschrift Fur Geophysik*, **49**, 89–92.

Barcilon V, Lovera OM (1989) Solitary waves in magma dynamics. *Journal of Fluid Mechanics*, **204**, 121–33.

Barcilon V, Richter FM (1986) Nonlinear-waves in compacting media. *Journal of Fluid Mechanics*, **164**, 429–48.

Bercovici D, Ricard Y, Schubert G (2001) A two-phase model for compaction and damage 1. General Theory. *Journal of Geophysical Research-Solid Earth*, **106**, 8887–906.

Birchwood RA, Turcotte DL (1994) A unified approach to geopressuring, low-permeability zone formation, and secondary porosity generation in sedimentary basins. *Journal of Geophysical Research*, **99**, 20051–8.

Brown M (2010) The spatial and temporal patterning of the deep crust and implications for the process of melt extraction. *Philosophical Transactions of the Royal Society of London Series A: Mathematical, Physical and Engineering Sciences*, **368**, 11–51.

Carman PC (1939) Permeability of saturated sands, soils and clays. *Journal of Agricultural Science*, **29**, 262–73.

Chauveau B, Kaminski E (2008) Porous compaction in transient creep regime and implications for melt, petroleum, and CO_2 circulation. *Journal of Geophysical Research-Solid Earth*, **113**, B09406.

Connolly JAD (1997) Devolatilization-generated fluid pressure and deformation-propagated fluid flow during prograde regional metamorphism. *Journal of Geophysical Research*, **102**, 18149–73.

Connolly JAD (2010) The mechanics of metamorphic fluid expulsion. *Elements*, **6**, 165–72.

Connolly JAD, Podladchikov YY (1998) Compaction-driven fluid flow in viscoelastic rock. *Geodinamica Acta*, **11**, 55–84.

Connolly JAD, Podladchikov YY (2000) Temperature-dependent viscoelastic compaction and compartmentalization in sedimentary basins. *Tectonophysics*, **324**, 137–68.

Connolly JAD, Podladchikov YY (2004) Fluid flow in compressive tectonic settings: Implications for mid-crustal seismic reflectors and downward fluid migration. *Journal of Geophysical Research*, **109**, B04201.

Connolly JAD, Podladchikov YY (2007) Decompaction weakening and channeling instability in ductile porous media: Implications for asthenospheric melt segregation. *Journal of Geophysical Research*, **112**, B10205.

Connolly JAD, Podladchikov YY (2013) A hydromechanical model for lower crustal fluid flow. In: *Metasomatism and the Chemical Transformation of Rock* (eds Harlov DE, Austrheim H), pp. 599–658. Springer, Berlin.

Etheridge MA, Wall VJ, Cox SF, Vernon RH (1984) High fluid pressures during regional metamorphism and deformation – implications for mass-transport and deformation mechanisms. *Journal of Geophysical Research*, **89**, 4344–58.

Forsyth DW, Scheirer DS, Webb SC, Dorman LM, Orcutt JA, Harding AJ, Blackman DK, Morgan JP, Detrick RS, Shen Y, Wolfe CJ, Canales JP, Toomey DR, Sheehan AF, Solomon SC, Wilcock WSD, Team MS (1998) Imaging the deep seismic structure beneath a mid-ocean ridge: The MELT experiment. *Science*, **280**, 1215–8.

Fowler A (1984) A mathematical model of magma transport in the asthenosphere. *Geophysical and Astrophysical Fluid Dynamics*, **33**, 155–90.

Fowler AC, Yang X (1999) Pressure solution and viscous compaction in sedimentary basins. *Journal of Geophysical Research*, **104**, 12989–97.

Gavrilenko P, Gueguen Y (1993) Fluid overpressures and pressure solution in the crust. *Tectonophysics*, **21**, 91–110.

Gliko AO, Singh RN, Swathi PS (1999) Physical approach to the problem of origin of charnockitic rocks of southern India: Mechanisms of crustal heating and transfer of carbon dioxide. *Russian Journal of Earth Sciences*, **1**, 409–21.

Gratier JP, Favreau P, Renard F (2003) Modeling fluid transfer along California faults when integrating pressure solution crack sealing and compaction processes. *Journal of Geophysical Research-Solid Earth*, **108**, B02104.

Gueguen Y, Dormieux L, Bouteca M (2004) Fundamentals of poromechanics. In: *Mechanics of Fluid-Saturated Rocks* (eds Gueguen Y, Bouteca M), pp. 55–79. Elsevier Academic Press, Burlington.

Hanson RB (1997) Hydrodynamics of regional metamorphism doe to continental collision. *Economic Geology and the Bulletin of the Society of Economic Geologists*, **92**, 880–91.

Helfrich KR, Whitehead JA (1990) solitary waves on conduits of buoyant fluid in a more viscous-fluid. *Geophysical and Astrophysical Fluid Dynamics*, **51**, 35–52.

Holtzman BK, Groebner NJ, Zimmerman ME, Ginsberg SB, Kohlstedt DL (2003) Stress-driven melt segregation in partially molten rocks. *Geochemistry Geophysics Geosystems*, **4**, 8607.

Hunt JM (1990) Generation and migration of petroleum from abnormally pressured fluid compartments. *American Association of Petroleum Geologists*, **74**, 1–12.

Ingebritsen SE, Manning CE (1999) Geological implications of a permeability-depth curve for the continental crust. *Geology*, **27**, 1107–10.

Japsen P, Dysthe DK, Hartz EH, Stipp SLS, Yarushina VM, Jamtveit B (2011) A compaction front in North Sea chalk. *Journal of Geophysical Research-Solid Earth*, **116**, B11208.

Joshi A, Appold MS, Nunn JA (2012) Evaluation of solitary waves as a mechanism for oil transport in poroelastic media: A case study of the South Eugene Island field, Gulf of Mexico basin. *Marine and Petroleum Geology*, **37**, 53–69.

Kameyama M, Yuen DA, Karato SI (1999) Thermal-mechanical effects of low-temperature plasticity (the Peierls mechanism) on the deformation of a viscoelastic shear zone. *Earth and Planetary Science Letters*, **168**, 159–72.

Katz RF (2008) Magma dynamics with the enthalpy method: Benchmark solutions and magmatic focusing at mid-ocean ridges. *Journal of Petrology*, **49**, 2099–121.

Kohlstedt DL, Evans B, Mackwell SJ (1995) Strength of the lithosphere – constraints imposed by laboratory experiments. *Journal of Geophysical Research-Solid Earth*, **100**, 17587–602.

McKenzie D (1984) The generation and compaction of partially molten rock. *Journal of Petrology*, **2**, 713–65.

McKenzie D (1987) The compaction of igneous and sedimentary rocks. *Journal of the Geological Society*, **144**, 299–307.

Miller SA, Collettini C, Chiaraluce L, Cocco M, Barchi M, Kaus BJP (2004) Aftershocks driven by a high-pressure CO_2 source at depth. *Nature*, **427**, 724–7.

Milord I, Sawyer EW, Brown M (2001) Formation of diatexite migmatite and granite magma during anatexis of semi-pelitic metasedimentary rocks: An example from St. Malo, France. *Journal of Petrology*, **42**, 487–505.

Nabelek PI (2009) Numerical simulation of kinetically-controlled calc-silicate reactions and fluid flow with transient permeability around crystallizing plutons. *American Journal of Science*, **309**, 517–48.

Neuzil CE (1994) How permeable are clays and shales? *Water Resources Research*, **30**, 145–50.

Neuzil CE (2003) Hydromechanical coupling in geologic processes. *Hydrogeology Journal*, **11**, 41–83.

Norton D, Knapp R (1977) Transport phenomena in hydrothermal systems – nature of porosity. *American Journal of Science*, **277**, 913–36.

Nye JF (1953) The flow law of ice from measurements in glacier tunnels, laboratory experiments and the Jungfraufirn borehole experiment. *Proceedings of the Royal Society of London Series A: Mathematical and Physical Sciences*, **219A**, 477–89.

Olson P, Christensen U (1986) Solitary wave-propagation in a fluid conduit within a viscous matrix. *Journal of Geophysical Research-Solid Earth and Planets*, **91**, 6367–74.

Rabinowicz M, Vigneresse JL (2004) Melt segregation under compaction and shear channeling: Application to granitic magma segregation in a continental crust. *Journal of Geophysical Research-Solid Earth*, **109**, B04407.

Rabinowicz M, Ricard Y, Gregoire M (2002) Compaction in a mantle with a very small melt concentration: Implications for the generation of carbonatitic and carbonate-bearing high alkaline mafic melt impregnations. *Earth and Planetary Science Letters*, **203**, 205–20.

Ranalli G (1995) *Rheology of the Earth*. Springer-Verlag, New York.

Revil A, Cathles LM (2002) Fluid transport by solitary waves along growing faults – a field example from the South Eugene Island Basin, Gulf of Mexico. *Earth and Planetary Science Letters*, **202**, 321–35.

Rice JR (1992) Fault stress states, pore pressure distributions, and the weakness of the San Andreas fault. In: *Fault Mechanics and Transport Properties of Rocks* (eds Evans B, Wong T-F), pp. 475–503. Academic Press, NY.

Richard GC, Kanjilal S, Schmeling H (2012) Solitary-waves in geophysical two-phase viscous media: A semi-analytical solution. *Physics of the Earth and Planetary Interiors*, **198**, 61–6.

Richter FM, McKenzie D (1984) Dynamical models for melt segregation from a deformable rock matrix. *Journal of Geology*, **92**, 729–40.

Sawyer EW (1998) Formation and evolution of granite magmas during crustal reworking: the significance of diatexites. *Journal of Petrology*, **39**, 1147–67.

Scott DR, Stevenson DJ (1984) Magma solitons. *Geophysical Research Letters*, **11**, 1161–4.

Scott DR, Stevenson DJ (1986) Magma ascent by porous flow. *Journal of Geophysical Research-Solid Earth and Planets*, **91**, 9283–96.

Scott DR, Stevenson DJ, Whitehead JA (1986) Observations of solitary waves in a viscously deformable pipe. *Nature*, **319**, 759–61.

Shi Y, Wang C (1986) Pore pressure generation in sedimentary basins: overloading versus aquathermal. *Journal of Geophysical Research*, **91**, 2153–62.

Sibson RH (1992) Fault-valve behavior and the hydrostatic lithostatic fluid pressure interface. *Earth-Science Reviews*, **32**, 141–4.

Simpson GDH (1998) Dehydration-related deformation during regional metamorphism, NW Sardinia, Italy. *Journal of Metamorphic Geology*, **16**, 457–72.

Spiegelman M (1993) Physics of melt extraction – theory, implications and applications. *Philosophical Transactions of the Royal Society of London Series A: Mathematical, Physical and Engineering Sciences*, **342**, 23–41.

Staude S, Bons PD, Markl G (2009) Hydrothermal vein formation by extension-driven dewatering of the middle crust: An example from SW Germany. *Earth and Planetary Science Letters*, **286**, 387–95.

Stevenson D (1989) Spontaneous small-scale melt segregation in partial melts undergoing deformation. *Geophysical Research Letters*, **16**, 1067–70.

Suetnova EI, Carbonell R, Smithson SB (1994) Bright seismic reflections and fluid movement by porous flow in the lower crust. *Earth and Planetary Science Letters*, **126**, 161–9.

Sumita I, Yoshida S, Kumazawa M, Hamano Y (1996) A model for sedimentary compaction of a viscous medium and its application to inner-core growth. *Geophysical Journal International*, **124**, 502–24.

Tenthorey E, Cox SF (2006) Cohesive strengthening of fault zones during the interseismic period: An experimental study. *Journal of Geophysical Research-Solid Earth*, **11**, B09202.

Tian M, Ague JJ (2014) The impact of porosity waves on crustal reaction progress and CO_2 mass transfer. *Earth and Planetary Science Letters*, **390**, 80–92.

Tumarkina E, Misra S, Burlini L, Connolly JAD (2011) An experimental study of the role of shear deformation on partial melting of a synthetic metapelite. *Tectonophysics*, **503**, 92–9.

Vigneresse JL, Barbey P, Cuney M (1996) Rheological transitions during partial melting and crystallization with application to felsic magma segregation and transfer. *Journal of Petrology*, **37**, 1579–600.

Wiggins C, Spiegelman M (1995) Magma migration and magmatic solitary waves in 3-D. *Geophysical Research Letters*, **22**, 1289–92.

Wilkinson DS, Ashby MF (1975) Pressure sintering by power law creep. *Acta Metallurgica*, **23**, 1277–85.

Yarushina VM (2009) (De)compaction waves in porous viscoelastoplastic media, PhD Thesis. University of Oslo, Oslo.

Zhu W, David C, Wong T-F (1995) Network modeling of permeability evolution during cementation and hot isostatic pressing. *Journal of Geophysical Research*, **100**, 15451–64.

Zhu W, Evans B, Bernabe Y (1999) Densification and permeability reduction in hot-pressed calcite: A kinetic model. *Journal of Geophysical Research-Solid Earth*, **104**, 25501–11.

Zoback MD, Townend J (2001) Implications of hydrostatic pore pressures and high crustal strength for the deformation of intraplate lithosphere. *Tectonophysics*, **336**, 19–30.

APPENDIX: NON-DIMENSIONALIZATION

For typical constitutive relations, the compaction equations admit a dimensionless form in the small porosity limit ($1 - \phi \to 1$, $\phi_d - \phi \to \phi_d$) that is independent of the absolute porosity (Scott & Stevenson 1984). In this limit, the constitutive relations given by Eqs 17 and 19 are

$$k = a_\phi \phi^{n_\phi} \tag{67}$$

$$f_\phi = n_\sigma^{-n_\sigma} (3/2)^{n_\sigma+1} \phi^{m_\sigma}. \tag{68}$$

Making use of these relations, and substituting $v_\phi = -v_\infty$, the dimensional forms of Eqs 15 and 16 simplify to

$$\frac{\partial p_o}{\partial z} = -v_\phi \frac{\eta_f}{k}(\phi - \phi_0) - \Delta\rho g\left(1 - \left[\frac{\phi_0}{\phi}\right]^{n_\phi}\right) \tag{69}$$

and

$$\frac{\partial \phi}{\partial z} = -\left(\frac{3}{2}\right)^{n_\sigma+1} \frac{\phi^{m_\sigma}}{n_\sigma^{n_\sigma} v_\phi} A |p_o|^{n_\sigma - 1} p_o. \tag{70}$$

Taking the small porosity limit for the Darcy velocity through the unperturbed matrix

$$v_0 = -\frac{a_\phi \phi_0^{n_\phi - 1}}{\eta_f} \Delta\rho g, \tag{71}$$

ϕ_0, $|\Delta\rho g|$, and δ as characteristic scales for velocity, porosity, pressure gradient, and length, respectively, the non-dimensional wave velocity, porosity, overpressure, hydraulic potential, and depth are $v'_\phi = v_\phi / v_0$, $\phi\prime = \phi/\phi_0$, $p'_o = p_o/(\delta|\Delta\rho g|)$, $H' = H\phi_0^{m_\sigma - 1}/|\Delta\rho g|$, and $z' = z/\delta$. Inverting these relations to express the dimensional variables in terms of the scales and non-dimensional variables, the non-dimensional forms of Eqs 69 and 70 are

$$\frac{\partial p'_o}{\partial z'} = \left[1 + v'_\phi(\phi' - 1)\right]/\phi'^{n_\phi} - 1 \tag{72}$$

and

$$\frac{\partial \phi'}{\partial z'} = \left(\frac{3}{2}\delta\right)^{n_\sigma+1} \frac{a_\phi \phi_0^{n_\phi - m_\sigma}}{n_\sigma^{n_\sigma} |\Delta\rho g|^{n_\sigma - 1}} A \frac{\phi'^{m_\sigma} |p'_o|^{n_\sigma - 1} p'_o}{v'_\phi}. \tag{73}$$

Defining the compaction length scale as

$$\delta \equiv \sqrt[n_\sigma+1]{\frac{n_\sigma^{n_\sigma} a_\phi \phi_0^{n_\phi - m_\sigma}}{A\eta_f |\Delta\rho g|^{n_\sigma - 1}} \left(\frac{2}{3}\right)^{n_\sigma+1}} \tag{74}$$

Eq. 73 reduces to

$$\frac{\partial \phi'}{\partial z'} = \frac{\phi'^{m_\sigma} |p'_o|^{n_\sigma - 1} p'_o}{v'_\phi}. \tag{75}$$

The dimensionless hydraulic potential is then

$$H' = \int \frac{1 - [1 + v'_\phi(\phi' - 1)]/\phi'^{n_\phi}}{\phi'^{m_\sigma}} d\phi'. \tag{76}$$

The hydraulic potential and solitary wave solution in Fig. 2D–F are computed from Eqs 72, 75 and 76 with $m_\sigma = 0$, $n_\phi = 3$, and $v'_\phi = 7$.

GEOFLUIDS

Volume 15, Number 1 and 2, February 2015

ISSN 1468-8115

CONTENTS